A model of the methane cycle, permafrost, and hydrology of the Siberian continental margin

David Archer, University of Chicago

d-archer@uchicago.edu

Abstract

A two-dimensional model of a passive continental margin was adapted to the simulation of the methane cycle on Siberian continental shelf and slope, attempting to account for the impacts of glacial / interglacial cycles in sea level, alternately exposing the continental shelf to freezing conditions with deep permafrost formation during glacial times, and immersion in the ocean in interglacial times. The model is then subjected to a potential future climate warming scenario.

Pore fluid salinity plays a central role in the model geochemical dynamics. In the permafrost zone, pure water ice tolerates a higher fluid salinity than methane hydrate can, eliminating hydrate as an equilibrium phase. An analogous region in the ice – hydrate – brine phase diagram excludes ice in favor of hydrate, but the two phases can coexist at a sub-saturated methane concentration. In the permafrost zone (cold and low pressure), in contrast, the dissolved methane concentration cannot be higher than equilibrium with gas, so the hydrate exclusion from this zone is inescapable. This thermodynamic constraint restricts methane hydrate to at least 300 meters depth below the sediment surface, precluding a fast hydrate dissolution response to sea-floor warming.

The initial salinity of the sediment column may have been affected by previous hydrological forcing, because freshwater invasion driven by a pressure head is probably much faster than salinity invasion due to convective-diffusive processes. This has a ratcheting effect, leaving relict fresh water lenses below sea level in many parts of the world. The pore fluid salinity determines the relative volumes of the ice, brine, and hydrate phases in the sediment column, and therefore the timing of ice formation and melting, but the chemical composition, in particular the salinity of the brine phase, is fixed, in equilibrium, by the local

temperature. The model hydrate inventory on the shelf is however sensitive to the initial salinity of the sediment column.

Through the glacial / interglacial cycles, the atmospheric methane flux is affected most strongly by changes in sea level, because bubbles dissolve in the ocean when sea level is high. Methane emissions to the atmosphere are highest during the sea-level fall part of the cycle (as soil is freezing), rather than during the warming deglaciations. Timings of the atmospheric methane flux changes are sensitive to assumptions made about bubble transport inhibition by permafrost. The atmospheric flux is sensitive to biogenic and thermogenic methane production rates, but the hydrate inventory is only sensitive to thermogenic methane production. The geothermal heat flux affects the thickness of the hydrate stability zone (primarily the depth of its base), but not the inventory of hydrate in the model until a low-gradient threshold is passed. The model produces methane inventory changes of 50 Gton C as bubbles, and as much as hundreds of Gton C as hydrate, but these reservoir changes interact mostly with pore water dissolved methane rather than driving immediate methane loss from the sediment column.

The model-predicted methane flux to the atmosphere in response to a warming climate is small, relative to the global methane production rate, because of the ongoing flooding of the continental shelf. The atmospheric methane flux response to sudden warming takes thousands of years, because of the slow thermal diffusion time to the hydrate stability zone, and because a warming perturbation beginning now would follow a much larger warming perturbation that started thousands of years ago, when the sediment surface flooded. On time scales of thousands of years in the future, the increased methane flux increase due to warming could be completely counteracted by sea level rise, which decreases the efficiency of bubble transit through the water column.

1. Introduction

1.1 The Siberian Continental Shelf System

The Siberian Arctic continental shelf has been the focus of attention from scientists and the public at large for its potential to release methane, a greenhouse gas, in response to climate warming, a potential amplifying positive feedback to climate change [*Shakhova*, 2010; *Westbrook*, 2009]. The goal of this paper is to simulate the geophysical and carbon cycle dynamics of the Siberian continental margin within the context of a basin- and geologic time-scale mechanistic model of the coastal margin carbon cycle called SpongeBOB [*Archer et al.*, 2012]. An initial condition for the glacial cycle simulations was generated by spinning the up at low resolution over 62 million simulated years. Then the model at higher resolution is driven by cyclic changes in sea level and air temperature resulting from glacial cycles, to simulate the impact of the hydrological pressure head and permafrost formation on the fluid flow and methane cycle on the shelf. Finally, an 100,000-year interglacial interval in the simulation is subjected to anthropogenic warming of the overlying water and potential 60-meter changes sea level. Sensitivity studies are presented for the biogenic and thermogenic methane production rates, initial salinity, geothermal temperature gradient, rates of hydrological flow, and permafrost impact on gas mobility.

1.1.1 Permafrost

One component of the simulation is a wedge of frozen sediment (permafrost) submerged beneath the ocean on the continental shelf of Siberia, left behind from glacial time when the shelves were exposed to the frigid atmosphere by lowered sea level [*Romanovskii and Hubberten*, 2001]. The ice is thought to provide a seal to upward migration of methane gas [*Shakhova et al.*, 2009], especially where ancient fresh groundwater flow produced a layer of very high saturation ice infill, a formation called the Ice Complex in Siberia [*Romanovskii et al.*, 2000], although there are high ice saturations found in the Alaskan Arctic as well [*Zimov et al.*, 2006].

With inundation by the natural sea level rise over the last 10+ thousand years, the permafrost is transiently melting, although the time constant for this is generally long enough that significant frozen volume remains, especially in shallower waters which were flooded more recently [*Khvorostyanov et al.*, 2008a; *Nicolsky and Shakhova*, 2010; *Romanovskii and Hubberten*, 2001; *Romanovskii et al.*, 2004; *Shakhova et al.*, 2009; *Taylor et al.*, 1996]. Even overlying water at the freezing temperature can provoke subsurface melting by providing a warmer boundary condition against which geothermal heat establishes the subsurface temperature profile, but with climate warming, the waters could surpass the freezing temperature, allowing heat to flow from above as well as below [*Khvorostyanov et al.*, 2008b].

Elevated methane concentrations have been measured in the water column over the Siberian shelf, even in areas of shallow water where the permafrost should still be strongly intact [*Shakhova*, 2010; *Shakhova et al.*, 2005]. Chemical and isotopic signatures of hydrocarbons adsorbed onto surface sediments indicate a thermal origin [*Cramer and Franke*, 2005], suggesting that the methane is produced many kilometers deep in the sediment column. The apparent ability for this methane to transverse the barrier of the Ice Complex has been attributed to hypothesized openings in the ice (called “taliks”), resulting from lakes or rivers on the exposed shelf, or geologic faults [*Nicolsky and Shakhova*, 2010; *Romanovskii et al.*, 2004; *Shakhova et al.*, 2009].

1.1.2 Salt

Dissolved salt in the pore waters can have a strong impact on the timing of thawing permafrost [*Nicolsky and Shakhova*, 2010; *Shakhova et al.*, 2009]. When sea level drops and exposes the top of the sediment column to the atmosphere and fresh water, the salinity of the subsurface pore waters can be flushed out by hydrological groundwater flow, driven by the pressure head from the elevated terrestrial water table above sea level. The boundary between fresh and salty pore water tends to intersect the sediment surface at the water’s edge [*Moore et al.*, 2011]. From there, the boundary tends to dip landward, to a depth of approximately 40 meters below sea level for every 1 meter of elevation of the table water. The ratio of water table elevation to freshwater lens depth is driven by the relative densities of fresh and salt water, as the fluid seeks an isostatic balance in which the fresh water displaces an equal mass of salt water [*Verrjuit*, 1968].

The SpongeBOB model has been modified to simulate the processes responsible for these observations. We do not attempt to simulate a detailed outcropping history over 62 million-year spinup time of the sediment column, but rather demonstrate the general process by subjecting the nearly complete sediment column to a one-time sea level lowering, exposing the continental shelf to groundwater forcing. After a few million years, the sediment column subsides, due to compaction and absence of sediment deposition, resulting in a sediment column that has been considerably freshened by the atmospheric exposure. This freshening persists in the model for millions of years, because there is no corresponding “salt-water pump” during high sea-level stands. This behavior is consistent with the discovery of vast nearly fresh aquifers in currently submerged continental shelf regions around the world [*Post et al.*, 2013], left over from groundwater forcing during glacial time.

1.1.3 Carbon

Another component of the simulation is the Yedoma, deposits of wind-blown dust and organic carbon that accumulated on the coastal plains of exposed continental shelves during glacial times [*Zimov et al.*, 2006]. The deposits contain a substantial fraction of organic carbon, consisting of grass roots and remains, preserved by the freezing conditions. When they thaw, they begin to release CO_2 and methane to the atmosphere [*Dutta et al.*, 2006; *Schuur et al.*, 2008; *Zimov et al.*, 2006]. Oxidation of the carbon can give off enough heat to accelerate the melting driven by primary climate forcing [*Khvorostyanov et al.*, 2008b].

2. Model Description

2.1 Previously Published Model Formulation

SpongeBOB is a two-dimensional basin spatial-scale and geological time-scale model for the methane cycle in continental margin sediments. The model, configured for a passive margin basin, was described by Archer et al [2012], as applied to the Atlantic coast of the United States. The model attempts to "grow" a sediment column based on first principles or parameterizations of sediment and pore water physical and chemical dynamics. The approach integrates processes of the carbon and methane cycles within the evolving sediment column matrix, providing constraints to the rates and processes that may inform the response of the system to future changes in climate. Where model parameterizations or parameters are poorly constrained, sensitivity studies are used to assess which of the uncertainties are the most significant.

Sediment is delivered from the coast of the model as riverine material, and it settles according to a parameterization of grain size, with finer material advecting further offshore before deposition. The organic carbon concentration of the depositing material is determined in the model as a function of water depth at the time of sedimentation. Rather than attempt to simulate the complex biogeochemical dynamics of the ocean and surficial sediments (early diagenesis), the POC fraction and the H/C ratio of the organic matter are specified by a parameterization based on water depth to reproduce the observed patterns of sediment surface POC deposition, as a driver to the subsurface model.

The H/C ratio of the depositing organic matter limits the potential extent of methane production from the organic matter. The degradation rate of organic carbon is estimated based on its age, a relationship that captures many orders of magnitude of variability in the natural world [*Middelburg et al.*, 1997]. The reaction pathways presume a reactive intermediate H_2, which either reduces SO_4^{2-} if it is available or it reacts with DIC to produce methane. Isotopic fractionation of CO_2, CH_4, and radioiodine are simulated by maintaining parallel concentration fields of different isotopologs, and applying fractionation factors to the chemical kinetic rate constants or equilibrium conditions. Dissolved methane in the pore water has the potential to freeze into methane hydrate or degas into bubbles, depending on the temperature, pressure, salinity, and CH_4 concentration.

Sediment compaction drives pore fluid advection through the sediment column, but the fluid flow is also focused in some simulations by ad hoc vertical channels of enhanced permeability, to simulate in at least a qualitative way the impact of heterogeneity in the fluid flow on the characteristics of the tracer field. Methane hydrate is concentrated in these channels by focused upward flow, and the pore-water tracers in the channels resembles that of hydrate-bearing regions (in SO_4^{2-} concentration and 129-Iodine ages).

Most of the model configuration and formulation was described by Archer et al. [2012]. The new modifications required to simulate groundwater hydrological flow and permafrost formation are described in detail below.

2.2 Groundwater Hydrology

2.2.1 Pressure Head

When the sediment column is exposed to the atmosphere, the pressure field from the variable elevation of the water table (the pressure head) begins to affect the fluid flow. The pressure head for a fluid particle at the depth of the water table varies as

$$P_{head}(z) = g\int_{z}^{z_{wt}} \rho_{seawater} dz$$

where z_{wt} is the elevation of the water table. The pressure head at each depth in the domain is a function of the physical water table height above it and the density anomalies integrated from the water table to the depth of the point in question. The pressure head resulting from a varying water table can therefore be altered at depth by variations in pore fluid density driven by salinity or temperature.

2.2.2 Fluid Flow

The pressure head acts in concert with the excess pressure P_{excess} to drive horizontal Darcy flow through the sediment, as

$$u_{Darcy,i\rightarrow i+1} = \frac{k_{h,i} + k_{h,i+1}}{2\mu} \frac{\left(P_{excess,i} - P_{excess,i+1}\right) + \left(P_{head,i} - P_{head,i+1}\right)}{(\Delta x_i + \Delta x_{i+1})/2}$$

while the vertical flow in the model is driven only by compaction pressure

$$w_{Darcy,j\rightarrow j+1} = \frac{k_{v,j}}{\mu} \frac{P_{excess,j} - P_{excess,j+1}}{(\Delta z_j + \Delta z_{j+1})/2}$$

The value of P_{excess} is determined from the porosity and sediment load of the sediment in each grid box, as described in Archer et al [2012]. An assumed sediment rheology is used to calculate the load-bearing capacity of the solid matrix within a given grid cell. P_{excess} is calculated by assuming that the load of the solid phase overlying the grid cell that is not carried by the solid matrix must be carried by the P_{excess} in the fluid phase. When ice forms (described below), it leaves P_{excess} unchanged, but the flow is inhibited by scaling the permeability k by the decrease in fluid porosity.

In previous versions of the SpongeBOB model, the fluid flow was calculated explicitly, each time step, as a function of P_{excess} at the beginning of the time step. Numerical stability motivated a modification of the vertical flow to an implicit numerical scheme, which finds by iteration an internally consistent array of vertical flow velocities and resulting P_{excess} values from a time point at the end of the time step. Ocean and atmosphere models often use this methodology for vertical flow. A benefit to this change is stability in the vertical flow field, reducing numerical noise that can cause trouble with other aspects of the model such as ice formation. Implicit schemes can be more efficient computationally, but in this case the execution time is not improved by the implicit method, just the stability.

Note that the flow scheme in its formulation is entirely elastic, whereas in reality, pore fluid excluded by the pressure of a sediment column above sea level, for example, where it is uncompensated by buoyancy in seawater, should remain excluded when sea level rises again, like toothpaste from the tube. However, my attempts to embed this plastic behavior into an implicit solver failed to converge.

2.2.3 Water Table Depth

The model maintains z_{wt}, the elevation of the water table within the sediment column, as a continuous variable that ranges through the discreet vertical grid of the model. The formulation allows boxes to be empty of water or partially "saturated" at the top of the fluid column. In these simulations, however, the water table remained very close to the sediment surface, as unsaturated soil produced by subsurface flow is quickly replenished by hydrological recharge.

2.2.4 Canyons

The model as described so far represents a laterally homogeneous slab, a poor approximation for hydrology above sea level because of the formation of canyons and river networks in a real drained plateau. The depth of the water table in a river canyon is depressed, relative to the surroundings, to the depth of the canyon. The water table is higher in between the canyons because of recharge, and the difference in head drives lateral flow, the canyons acting to drain the sediment column.

The model formulation has been altered to represent this mechanics in a simplified way. Rather than expand the model into the full third dimension, the 2-D field of the model is held to represent the sediment column at a hypothetical ridge crest, as altered by an adjacent canyon. The canyon elevation is represented by z_{canyon}, and its width by a scale Δy_{canyon}. A cross-column flow velocity $v_{Darcy,j}$ is calculated as

$$v_{Darcy,j} = \frac{k_{h,j}}{\mu} \frac{\left(P_{head,canyon} - P_{head}\right)}{\Delta y_{canyon}}$$

where $P_{head,canyon}$ is the pressure head as a function of depth in the hypothetical canyon, calculated assuming that the water table outcrops at z_{canyon}, and that the temperatures in the sediment column have adjusted to the formation of the canyon, such that the near-surface geothermal gradient is the same between the hypothetical canyon and the bulk sediment column. The lateral "drainage" flow ($v_{Darcy,j}$) drives vertical velocities by continuity.

The horizontal distance scale Δy_{canyon} is somewhat arbitrary and difficult to constrain, given that in the reality of river networks the distance to the nearest canyon from any point in the domain is likely to be a function of altitude, distance from the coast, and time. Another poorly resolved factor is the depth of the canyon. In reality, canyons cut into a plateau following a dynamic that erosion is proportional to slope, but stops at sea level. As a simplification the model is set to hold the canyon depth at current sea level.

The canyon mechanism accelerates the freshening of the sediment column by providing a pathway for the escape of the salt water, although it was found that the net effect in the model is not dramatic (results shown below), in part because the canyon drainage mechanism only acts on pore fluids above sea level, while the hydrological freshwater pumping mechanism reaches much deeper than sea level. In the real fractal geometry of canyons, the spacing between canyons across a plain is similar to the width of the plain (length of the canyons), so the Base simulation assumes a canyon width of 100 km, based on the 100+ km width scale of the continental shelf.

2.3 Permafrost

The ice model is based on an assumption of thermodynamic equilibrium, in which the heat content of the cell is distributed between the pure ice, hydrate, and brine phases, and the salinity of the brine drives a freezing point depression to match the local temperature. The ice content in a grid cell relaxes toward equilibrium, quickly enough to approximate an equilibrium state through the slow temperature evolution in the model (which neglects a seasonal cycle at the surface), but slowly enough to avoid instabilities with other components of the model such as fluid flow and methane hydrate formation. A limiter in the code prevents more than 99% of the fluid in a grid cell from freezing, but the thermodynamic equilibrium salinity is used to calculate, for example, the stability of methane hydrate, to prevent the numerical limiter from affecting the thermodynamic availability of water to drive chemical reactions.

This model formulation implies that the salinity of pore fluid in subfreezing conditions (the permafrost zone) is independent of the original salinity of the bulk sediment column, but is rather determined only by the freezing-point depression implied by the temperature. If the original column is relatively fresh, there will be a smaller volume of pore fluid at a subfreezing temperature than if it is originally salty (see for example Figure 4 in [*Nicolsky and Shakhova*, 2010]), but the activity of the water (a correlate of the salinity) is set by the temperature and the thermodynamics of pure ice, which are the same in the two cases. Layers of high-salinity unfrozen brines called cryopegs [*Gilichinsky et al.*, 2005; *Nicolsky et al.*, 2012] are consistent with this formulation.

2.4 Thermodynamic competition between ice and hydrate

The high salinity (low activity of water) in the permafrost zone has the practical impact of excluding methane hydrate from permafrost soils that are significantly colder than freezing. The thermodynamics are illustrated in Figure 1. When the system consists only of ice and fluid phases, the equilibrium salinity S_{eq} increases with decreasing temperature below freezing (Figure 1a, left). Above the melting temperature, ice is unstable, as indicated by the nonzero values of the disequilibrium temperature, $\Delta T_{eq,\ ice} = T - T_{eq,\ ice}$, in contours, even in zero-salinity water (right). For a system consisting of only the hydrate and fluid phases (assuming that ice formation is disallowed, and also gas saturation for methane) (Figure 1b), the behavior is similar but with an added pressure dependence due to the compressibility of the gas phase. When both solid phases are allowed, the overall equilibrium salinity will whichever is higher between $S_{eq,\ ice}$ and $S_{eq\ hydrate}$. Whichever phase can seize water at its lowest activity (highest salinity) will be the stable phase. The salinity of the brine excluded from that phase will be too high to permit the existence of the other solid phase at that temperature. The contours show ΔT_{eq} for hydrate (solid) and ice (dashed), which are also plotted in color in Figures 1d and e. This is illustrated in Figure 1d, in colors of $\Delta T_{eq,\ hydrate}$ and contours of the excess salinity relative to hydrate equilibrium, S_{max} - $S_{eq,\ hydrate}$. Hydrate is only stable when $\Delta T_{eq,\ hydrate}$ is zero (purple color). Under permafrost conditions of low pressure and low temperature (upper left corner), $\Delta T_{eq,\ hydrate}$ is greater than zero, indicating that hydrate is unstable, coinciding with the salinity forcing from the ice, in overlain contours. A similar exclusion of ice in part of the hydrate stability zone is seen Figure 1e, but this would only happen in nature in conditions of unlimited methane. The resulting phase diagram for ice and methane hydrate is shown in Figure 1f. Hydrate stability is suppressed in the permafrost zone by this thermodynamic mechanism.

Permafrost formation has several impacts on the methane cycle in the model. Biogenic methanogenesis is assumed stopped in the ice fraction of a grid cell (which approaches unity but never reaches it in the model, due to exclusion of salt into brine). Bubble transport in the model balances bubble production, driven by a small and not very well constrained standing bubble concentration within the pore space. It is generally assumed [*Shakhova et al.*, 2010b] that permafrost inhibits gas transport through the sediment column, both based on sediment column carbon and hydrogen budgets [*Hunt*, 1995] and on the tight seal provided by the ice complex. The seal provided to Arctic lakes, which can drain overnight if the seal is breached, also lends credence to this idea. In the model, this effect was simulated by stopping gas transport completely when a grid cell exceeds 50% ice fraction (with sensitivity runs assuming 10%, 30%, 70%, and 90%).

2.5 Atmospheric Methane Fluxes

Bubbles emerging from the sediment column into the water column of the ocean may dissolve in the water column, or they may reach the sea surface, a direct methane flux to the atmosphere [*Westbrook et al.*, 2009]. In the model, bubble dissolution in the water column is assumed to attenuate the bubble flux according to the water depth with an e-folding attenuation scale of 30 meters [*Gentz et al.*, 2014; *Portnov et al.*, 2013; *Westbrook et al.*, 2009]. In reality, a low-flux gas seep, producing small bubbles, will probably not reach as far into the water column as a 30-meter scale height, while a faster seep can reach further. Methane dissolved in the water column, in reality, may survive oxidation (time constant of about a year), and degas to the atmosphere, but this possibility is not included in the model. For land grid points (exposed to the atmosphere by lowered sea level), any upward bubble flux at the sediment surface is assumed 100% released to the atmosphere. The model neglects methane oxidation in soils, as well as many other terrestrial processes such as thaw bulbs beneath bodies of water [*Walter et al.*, 2006], and the seasonal cycle of melting and thawing in the surface active layer. In short, the methane fluxes to the atmosphere computed from the model runs are crude, and underlain by a sedimentary methane cycle with large uncertainties, intended to capture the main sensitivities to various processes rather than to provide strong quantitative constraint to the fluxes in the real world.

2.6 Comparison with Previous Models

The dynamics of the permafrost layer, and its present state, have been extensively modeled within detailed maps of the crust and sediment structure [*Gavrilov et al.*, 2003; *Nicolsky and Shakhova*, 2010; *Nicolsky et al.*, 2012; *Romanovskii and Hubberten*, 2001; *Romanovskii et al.*, 2005]. The crust underlying the continental shelf area has been alternately rising and subsiding in blocks called horsts and grabens [*Nicolsky et al.*, 2012]. The sediment cover on the grabens is much thicker than it is in the horsts. SpongeBOB, an idealized two-dimensional model, does not address this complexity, but the thickness of the sediment cover on the shelf ranges from 5 – 10 kilometers, reminiscent of the grabens (subsiding blocks). A thin sediment column would not reach the temperature required for thermogenic methane production. The rates of thermogenic methane production are not predicted or constrained by the model, because of the different depositional histories of the sediment columns. However, we can gauge the sensitivity of the methane cycle in the near-surface sediments to thermogenic methane production by scaling the model-predicted rate (by factors of 10 and 100).

Methane hydrate modeling has been done in the Arctic applied to the Siberian continental slope [*Reagan*, 2008; *Reagan and Moridis*, 2009; *Reagan et al.*, 2011], but only one calculation has been done in the context of permafrost formation [*Romanovskii et al.*, 2005], as found on the shelf. Romanovski [2005] modeled the extent of the methane hydrate stability zone through glacial cycles, but based the calculations on marine salinity values when calculating the stability of hydrate, while I argue that in sub-freezing conditions (in the permafrost zone) the only water available for hydrate formation will be in a saline brine that would be in equilibrium with ice at the local temperature. This formulation restricts hydrate stability from the permafrost zone to greater depth below the sea floor than predicted by Romanovski [2005]. In the Mackenzie Delta, hydrate was detected in a core drilled into onshore permafrost soils [*Dallimore and Collett*, 1995], but only at depths greater than 300 meters, near the base of the permafrost zone.

3. Results

3.1 Initial Spinup

The point of the spinup phase is to generate an initial condition for the glacial cycle simulations. The more usual approach in modeling hydrates is to start with an ad-hoc initial condition [*Reagan*, 2008; *Reagan and Moridis*, 2009; *Reagan et al.*, 2011]. For SpongeBOB the model state at any time is the result of the time-history of sedimentation, which is driven by the time-evolving depth of the sea floor, and interacting with isostatic adjustment of the crust. The simplest way to generate an initial condition in the model without a startup transient is to spin the model up from bedrock at low resolution. Because of the over-simplicity of the tectonic, sea level, and sedimentation forcing of the spinup phase, its POC concentrations and methane production rates do not constrain those of the real Siberian shelf. The sensitivity of the glacial methane cycles to methane production rates will be evaluated by scaling the model methanogenesis rates from the spinup result. The model setting was grown for 62 million years of model time. The initial spinup used a relatively coarse resolution as shown in Figure 2a.

For the glacial / interglacial experiments, the initial condition was interpolated to a higher resolution grid in the vertical, as shown in Figure 2b. Particulate organic carbon (POC) concentrations are highest just off the shelf break (Figure 3), because this is where most of the sediment is deposited, and because the sedimentary material is richest in POC in shallow ocean water depths [*Archer et al.*, 2012]. The unchanging sea level in the spinup period kept the sediment surface from outcropping, resulting in nearly uniform marine salinity throughout the model domain (Figure 4a). Methane concentration (Figure 5a) closely mirrors the solubility of dissolved methane, resulting in near saturation concentrations through most of the model domain (Figure 5b). As in the previous model simulations [*Archer et al.*, 2012], the imposition of permeable channels has a strong effect on the chemistry of the permeable grid cells (Figure 5d), although the impact on the integrated model behavior, such as the methane flux to the atmosphere, was small in these simulations.

3.2 Impact of Freshwater Hydrology

When sea level drops such that the surface of the sediment column outcrops to the atmosphere, the pore fluid becomes subject to the pressure head driving it seaward, and to fresh water recharge from precipitation. The pressure head forcing and the buoyancy of the sediment fluid column combine to create a mechanism to excavate salinity from the upper sediment column. Initially after sea level fall, there is a pressure head gradient extending throughout the sediment column, provoking lateral flow at all depths. As the pore fluid at the surface is replaced by fresh runoff, the lighter density of that fluid tends to diminish the pressure head gradient in the deeper sediment column. The deeper pressure gradient and flow approach zero as the fresh water lens in the outcropping region approaches an isostatic equilibrium condition known as the Ghyben-Herzberg relation [*Moore et al.*, 2011], in which each meter elevation of the water table is compensated for by about 40 meters of fresh water below sea level, determined by the difference in densities of fresh and salt water.

To create this condition within the model, two simulations are presented in which sea level was decreased by 30 and 120 meters, respectively, and held there for millions of years (Figure 6). The 30-meter drop experiment produced land outcrop in about 1/4 of the model domain, with the predicted equilibrium Ghyben-Herzberg halocline reaching about 1200 meters maximum depth. The model salinity relaxes into close agreement with the predicted halocline, lending support to the model formulation for density, pressure head, and fluid flow. As time progresses further, the outcropping land surface subsides (there is no land deposition in this scenario), until it drops below the new lowered sea level value after about 2.5 Myr.

Variants of this experiment were done with differing values of the lateral distance to drainage canyons in the model, which provide a pathway for fluid loss in sediments above sea level. When a hypothetical canyon is located 10 km from the SpongeBOB slab, the model salinity approaches equilibrium on an e-folding time scale of about 400 kyr (Figure 7). When the canyon is 100 km distant or nonexistent, the equilibration time scale is about 600 kyr. Based on the idea that canyons of order 100 km long should be about 100 km apart, the Base simulation in this paper assumes canyon spacing of 100 km.

When sea level is lowered by 120 m, the sequence of events is similar, except that the pressure head is so high that to satisfy the Ghyben-Herzberg relation would require fresh pore waters at many kilometers depth, even deeper than bedrock on the “continental” side of the model domain. Because of the low permeability of the deepest sediment column, the freshwater pumping groundwater mechanism is unable to reach these deepest pore waters, which therefore remain salty. The time scale for establishing a significant freshening of the upper kilometer of the sediment column is still on the order of 100-500 kyr, and the subsequent subsidence time of the sediment column in the model, until it drops below the new lowered sea level, takes about 10 Myr. In both cases, subsidence of the exposed sediment column prevents the sediment surface in the model from remaining above sea level indefinitely (without land deposition).

The sequence of events leaves behind a fresh water lens below sea level that persists in the model for millions of years (Figure 6). Groundwater flow, driven by the pressure head, provides an advective means of pumping fresh water into the subsurface sediment column that has no counterpart for salty ocean water. The model lacks the mechanism of salt fingering, which can enhance the diffusion of salt from above into a fresh water aqufer [*Kooi et al.*, 2000]. However, higher-resolution models of smaller domains that accounted for salt fingering also show a time asymmetry, with faster fresh water invasion on sea level drop than salt invasion on sea level rise [*Lu and Werner*, 2013; *Watson et al.*, 2010]. As the size of the domain increases with increasing sea level change, advective processes such as hydrological flow should become even more dominant over diffusive processes such as salt fingering. The recent discovery of vast freshwater aquifers on global continental shelves [*Post et al.*, 2013], persisting since the time of lowered sea level 20,000 years ago, and the lower-than-marine salinities of the pore waters measured in submerged surface Arctic sediments (summarized by [*Nicolsky et al.*, 2012]) are also consistent with the existence of a fresh-water hydrological pump which has a significant impact on sediment column salinities. The hydrological pumping generates a low-methane plume that also persists for millions of years in the model (Figure 8). Two states, called “prefreshened” and “pure marine”, serve as end-member initial conditions for glacial / interglacial simulations (Figure 4b), to evaluate the sensitivity of the model glacial cycles to the initial salinity of the sediment column.

3.3 Glacial Cycles

3.3.1 Setup and Forcing

Beginning from an entirely submerged initial condition, the model is subjected to 100-kyr sawtooth cycles of sea level ranging between –120 to +20 meters from the initial sea level (starting at –120 for prefreshened, 0 for pure marine) (Figure 9a).

The model scenarios and sensitivity studies are summarized in Table 1.

The simplest scenario (SL) varies the sea level while keeping the air and water temperatures time-invariant. The sea-level air temperature is maintained at 0 °C. This simulation is nearly permafrost-free, with a small exception where the altitude of the sediment surface is much higher than sea level (due to the lapse rate in the atmosphere). There is no deposition of sediment above sea level in this simulation. Permafrost formation is added in simulation GL, in which the air temperature ramps down to -16 °C at sea level, linearly with the glacial sea level fall (Figure 9b). In the ocean, shelf waters are always –1.8 °C, but an interglacial subsurface temperature maximum of 1 °C at 200 meters decreases to –1.8 °C during glacial times. Deposition of organic-rich sediments when the surface is exposed to the atmosphere (Yedoma: represented as accumulation of 10 meters in 100 kyr, with 30% POC) is added in scenarios SL+LD and GL+LD (LD for land deposition). The atmospheric temperature impact of a global warming scenario (GW) is also shown in Figure 9b, beginning at 400 kyr, and compared with an extended-interglacial control forcing (Ctl). The potential impact of geologic-time scale sea level rise is added to the global warming scenario in simulation GL+SL.

Other model sensitivity runs used varying values of the thermogenic and biogenic methane production rates, the geothermal temperature gradient. Several altered-physics runs were done, one adding vertical permeable channels, one disabling horizontal flow, and several to evaluate the impact of ice formation on methane hydrate stability.

3.3.2 Salinity and Ice

In the “prefreshened” initial condition (Fr), millions of years have elapsed since the previous exposure of the sediment to hydrological forcing, but a core of fresh water remains. Salinities near the sediment surface have grown saltier due to diffusive contact with seawater (Figure 10, left). A fully marine initial condition (Mar) (Figure 10, right) was initialized from the unfreshened case, in which sea level was held at a fixed value throughout the 65 Myr spinup of the sediment column. The salinities are nearly uniform in this case.

When the sediment surface is re-exposed to the atmosphere during an interval of sea level, in the absence of ice formation (simulation SL), the surface layer tends to freshen relatively quickly due to the hydrological forcing, but a subsurface salinity maximum persists (Figure 10c and d). However, if the air temperatures are cold enough to form ice (simulation GL), surface salinities in the model increase to up to nearly 190 psu, in both prefreshened and pure marine cases (Figure 10e and f). By the next interglacial time (Figure 10g and h), ice near the sediment surface has melted enough for near-surface pore waters to reach relatively low salinities.

3.3.3 Pressure and Flow

The effect of the sea level and permafrost forcing on the pressures and flow velocities are shown in Figure 11. On a spatial scale of the entire model domain (Figure 11, left), the highest driving pressures are found at the base of the sediment column, underneath the region of maximum sediment accumulation (the depocenter just off the shelf break). Changes in sea level drive large fluctuations in the pressure head (contours) extending to bedrock. In the near-surface continental shelf (Figure 11, right), the driving pressure variations are dominated by the pressure head driven by sea level changes. The formation of permafrost (GL, Figure 11 e and f) seals the upper sediment column to fluid flow. When sea level rises again, in the model configuration including permafrost, there is a strong pulse of downward flow following partial melting of the permafrost (Figure 11 h). It is possible that this flow, which lasts a few thousand years, is an artifact of the elastic model configuration, in which the release of a load (by submergence of the upper sediment column into the ocean) provokes the expansion of pore spaces in the sediment. The anomalous flow, integrated over its duration, could displace the pore fluid by about 40 meters, which is less than one grid cell. The model configuration without the sealing effect of permafrost (SL) does not show this pulse of invasive flow on sea level rise.

3.3.4 Methane Cycle

There are multiple ways in which the glacial cycles of sea level and air and water temperature might impact the flux of methane to the atmosphere. Submergence in the ocean is one modulating factor, because the emerging bubbles dissolve in the ocean rather than reaching the atmosphere. Another factor is the deposition of high-POC surface soils during low sea level stands, and its exposure to degradation later when the permafrost soils melt. A third factor is permafrost, impeding gas and fluid flow and excluding dissolved methane and salt from ice formation. The impacts of these processes are assessed by comparing the results from model configurations with and without each process in question.

The impact of phase competition between ice and hydrate is shown in Figure 12. In the Base scenario (Figure 12a and c) hydrate stability is excluded from the permafrost zone as described above and in Figure 1. Preventing ice from forming in an altered-physics simulation (+ No Ice) decreases the fluid-phase salinity relative to the Base simulation, and allows the methane hydrate stability zone to nearly reach the sea floor (Figure 12b and d), during strongest glacial conditions. Another altered-physics simulation was done in which ice is allowed to form, but not affect the salinity as it drives methane hydrate stability (which was hard-wired to marine salinity). Methane hydrate is still unstable in the permafrost zone through most of the simulation (see movie files in supplemental material), indicating that thermal interaction must also have a strong impact on methane hydrate stability in the permafrost zone.

The evolution of the dissolved methane disequilibrium condition (CH_4 / $CH_{4\ sat}$) is shown in Figure 13. At the initiation of the glacial cycles, methane is undersaturated in near-surface sediments on the continental shelf, by diffusive contact with the methane-free ocean upper boundary condition. In the prefreshened sediment column scenario (Fr), methane concentrations in the depth range of 100-1000 meters are lower than in the marine case (Mar, Figure 13b), due to the ventilation by the hydrological pump (Figure 13a). Further freshening of the pore waters in the ice-free case (SL+LD) tends to deplete methane in the upper sediment column (Figure 13c-e), while methane exclusion from the permafrost ice leads to supersaturation in simulation GL+LD (Figure 13 f-h). The hydrate stability zone is somewhat expanded in the prefreshened sediment column relative to the marine case (Figure 13 g vs. h, heavy black contour).

Figure 14 shows snapshots of various aspects of the shelf carbon cycle, beginning from a prefreshened initial condition. Sections of POC concentration in Figure 14, left show the accumulation of POC-rich Yedoma deposits on land (Figure 14 g and j). The rate of methane production in the model (Figure 14, right) depends on temperature and organic carbon age, but it is also attenuated by permafrost formation in the model, scaling to zero in the completely frozen case. Methanogenesis rates are near zero in the permafrost zone during glacial time (Figure

14h), but partially recover during interglacial time (Figure 14k) even though permafrost is still present.

A zone of methane hydrate stability exists below the permafrost zone when permafrost is present, and some methane hydrate accumulates in that zone. The highest pore-fraction values are found near the continental slope, where the shelf stability field outcrops within the slope depocenter. Dissolved methane concentrations exceed saturation within the stability zone in the model (Figure 13), but the accumulation of methane hydrate (Figure 14, right) is limited by the rate of methane production.

Time series plots of the inventory of methane as hydrate on the shelf are shown in Figure 15. The integration cuts off at x=560 km to exclude the sediment depocenter on the continental slope. Hydrate inventories reach maximum values during deglaciations. There is more hydrate when the pore water is fresher, and there would be more if ice were excluded from forming (Figure 15a). The hydrate inventory is much more sensitive to thermogenic methane production, deep in the sediment column, than Yedoma deposition (Figure 15b). The impact of the geothermal heat flux is to change the depth of the bottom of the hydrate stability zone (Figure 12 e and f), but the impact is small on the hydrate inventory, unless the temperature gradient is so low that hydrate persists through the entire glacial cycle (Figure 15c). The hydrate forms from the dissolved methane pool, which exceeds 1000 Gton C in shelf porewaters of the model.

The impact of the glacial cycles on the methane pathway to the atmosphere in the model is shown in Figure 16. When sea level is high, the efficiency of bubble transport across the sediment-water interface reaching the atmosphere ranges from about 75% near the coast to about 10% at the shelf break (Figure 16a). Most of the methane flux from the sediment is located just off the shelf break (Figure 16e), where the escape efficiency is low, so not much methane makes it to the atmosphere during the interglacial. During glacial times, the sediment column is exposed to the atmosphere, and the escape efficiency in the model is 100% (Figure 16b). Permafrost inhibits the terrestrial methane flux (Figure 16i) relative to the case without permafrost (Figure 16f). During some deglaciations, the release of pent-up gas by permafrost degradation leads to a spike of excess methane flux to the atmosphere (Figure 16j-k relative to 16g-h).

Time series plots of the major fluxes of the methane cycle on the continental margin are shown in Figure 17. The methanogenesis rates in the model output are in units of moles per meter of coastline, since it is a 2-D model. We scale this up to the Siberian continental margin by assuming a width of 1,000 km. The area of the shelf is then $5 \cdot 10^{11}$ m^2, roughly comparable to the real shelf area of 460,000 km^2 [*Stein and Fahl*, 2000]. The biological rate of methane production on the continental shelf evolves through time in Figure 17b. Yedoma deposition (case SL+LD) tends to slowly increase the total shelf respiration rate in the model, relative to a case with no land deposition (case SL). The formation of permafrost, during glacial periods of case GL+LD, attenuates methaneogenesis by inhibiting biological activity in the frozen soil.

The solid regions in Figure 17 c-h are cumulative methane sinks for six different model scenarios, plotted underneath red lines showing biogenic methane production. In time average, where sinks balance sources, the colored areas should fill up the region below the red line.

Trapping of methane by impermeable permafrost leads to a spike of methane fluxes at the ends of deglaciations in simulations with permafrost (Figure 17 c and e). The spikes happen as sea level approaches its highest extent, stifling the offshore groundwater flow by decreasing the pressure head, but early in the interglacial time while permafrost is the most intact. The spikes are stronger for the first glacial cycles than the last, apparently due to long-term adjustment of the methane cycle on the shelf (a growing together of the production rate (red lines in Figure 17 c-f) and the various methane sinks (colored areas).

Permafrost formation blocks methane emission during times of low sea level. This can be seen in the collapse of the blue regions in Figure 17 c vs. d and e vs. f during times of low sea level. Blocking horizontal flow disrupts offshore flow, the only significant methane sink on the shelf during glacial periods (Figure 17h), resulting in somewhat higher deglacial spikes of methane emission than predicted by the models including transport. There is no direct link between ice fraction and methane oxidation in the model, which is driven only by coexisting concentrations of sulfate and methane, but the rate of methane oxidation also drops to negligible during glacial times in the simulations with permafrost (grey in Figure 17 c and e). The absolute rates of methane loss differ between the Prefreshened vs. Marine initial conditions, but this is in part due to differences in the width of the continental shelf between the two simulations. The patterns of the methane cycle are very similar, however, between the two cases, and also not much affected by the imposition of permeable vertical channels (Figure 17g).

atmospheric fluxes

Fluxes of methane to the atmosphere are shown in Figure 18. In the absence of permafrost (Figure 18 a and b), or assuming that bubble migration is blocked only if the ice fraction exceeds 90%, a condition rarely attained in the model (Figure 18e), the highest methane fluxes to the atmosphere are found during glacial (cold) times, rather than warm interglacials. This is due to dissolution of methane gas into the ocean when the sediment column is submerged. When permafrost blocks methane gas fluxes in the sediment column, the highest atmospheric fluxes are generally found during the time of early sea level fall, when unfrozen sediment is exposed to the atmosphere before it has a chance to freeze. The timing of the variations in atmospheric flux through the glacial cycles is very sensitive to the critical ice fraction for blocking gas transport (Figure 18e).

The impacts of the pore water salt inventory are most apparent during the time of sea level fall, with permafrost formation (red lines). The saltier sediment column takes about 20 kyr to choke off the methane flux to the atmosphere (Figure 18a), while the pre-freshened sediment column stops the methane flux more abruptly, in just a few thousand years (Figure 18b).

Atmospheric emissions also scale with methane production rates, generally maintaining the temporal patterns of emission as set by permafrost and submergence in the ocean.

3.4 Anthropogenic Global Warming

The global warming (GW) scenario begins from a high sea-level interglacial state, and raising the temperature following the climate impact of the "spike and long tail" time distribution of a slug of new CO_2 added to the atmosphere [*Archer et al.*, 2009] (Figure 8). There is a stage of fast atmospheric drawdown as CO_2 invades the ocean, but once the ocean, atmosphere, and land surface reach equilibrium (after a few hundred years), the CO_2 content of the entire biosphere begins to relax toward an initial "natural" value, on time scales of hundreds of thousands of years, by weathering reactions with carbonate and siliceous solid rocks. The net result is a CO_2 drawdown that can be expressed as the sum of several exponential functions in time, with time scales ranging from 10^2 – 10^6 years.

Changes in water column temperature are assumed equal to those of the atmosphere, following paleoceanographic reconstructions [*Martin et al.*, 2002] and long-term coupled ocean / atmosphere circulation model experiments [*Stouffer and Manabe*, 2003]. The GW scenario imposes this temperature change on the water column, relaxing toward equilibrium with the atmospheric CO_2 trajectory with a time constant of 100 years.

The effect of sea level rise is added to create a second global warming scenario GW+SL. On time scales of thousands of years the sea level response to changing global temperature is much stronger than the sea level response over the coming century, as prominently forecast by the IPCC. Reconstruction of sea level and global temperature covariation in the geologic past (glacial time to Eocene hothouse) reveals a covariation of 10-20 meters per °C [*Archer and Brovkin*, 2008]. The global warming with sea level scenario assumes an equilibrium sea level response of 15 meters / °C, which it relaxes toward with a time constant of 1000 years.

The atmospheric methane fluxes, shown in Figure 19, increase in the global warming (GW) model run, as they also do in the control (Ctl) simulation, which is essentially an extended but unwarmed interglacial period. The permafrost melts on a time scale of about 10,000 years for the GW simulation, and about 50,000 for the Ctl. The rates of methane production, and flux to the atmosphere, both increase with the loss of the permafrost, if there is no change in sea level. However, the new methane flux comes not as a sudden burst, but rather as a slow transition toward a new, higher, chronic release rate. When sea level is also changed (GW+SL), bubbles dissolve in the water column, which more than counteracts the increase in methane flux due to the extended interglacial (Ctl) or warming (GW) scenarios.

3.5 Summary of Model Sensitivity Studies

Sediment Porewater Salinity. Ice freezes until the salinity of the residual brine brings about a freezing point depression equal to the in situ temperature. A saltier initial sediment column will reach this condition with a lower ice fraction, its melting is accelerated, and its hydrate inventory is lower (Figure 18). The equilibrium salinity in the permafrost zone is not affected by the salt inventory of the column, only the relative volumes of the solid and fluid phases.

Methane Production Rates. The atmospheric flux increases with increases in either shallow, biogenic methane production, driven by deposition of Yedoma, and thermogenic methane production in the deep sediment column (Figure 19). Biogenic methane is produced too shallow in the sediment column to impact the inventory of methane hydrate (Figure 15). The timing through the glacial cycles of atmospheric methane emissions from these scenarios parallel each other, because they are controlled in common by the transport-blocking effects of permafrost and sediment submergence in the ocean.

Geothermal Temperature Gradient. When the heat flux is higher, the temperature gradient is steeper, pivoting about the sediment surface temperature, which is set by the ocean. The base of the methane hydrate stability boundary gets shallower, while the top remains at about the same depth, resulting in a thinning of the stability zone (Figure 12). The hydrate inventory through the glacial cycles however is not much affected, unless the heat flux gets small enough for hydrate to persist through the glaciations (Figure 15).

Ice vs. hydrate thermodynamic competition. When ice is included as a competing phase, it excludes methane hydrate from the low-pressure, very cold permafrost zone. The hydrate stability zone thins (from above and below in the model: Figure 12), and the hydrate inventory decreases (Figure 15). When ice formation is disallowed, the hydrate stability zone approaches the sediment surface during coldest glacial time, but by the time of an interglacial-based global warming climate perturbation, the stability zone boundary has retreated to several hundred meters below the sea floor, precluding a sudden hydrate dissolution response to a suddenly warming ocean.

Permafrost inhibition of gas migration. When the ice fraction of the model exceeds a critical threshold, gas migration is blocked. Changing the value of this threshold has a strong impact on the rates of methane emission during glacial versus interglacial times. This process is therefore a high priority for future model refinement.

Vertical flow heterogeneity. The chemistry of continental margin sediments in this model [*Archer et al.*, 2012] showed a strong sensitivity to flow heterogeneity, achieved by increasing the vertical permeability of every fifth grid cell. In the configuration presented here, the impact of the channels is much smaller. The dynamics of this simulation are thermally driven, rather than by sediment deposition driving fluid flow in the continental margin case. Atmospheric methane fluxes are spikier when the channels are included, but the mean rate is not much changed.

Ground water flow. Groundwater flow carries enough methane to be a significant sink during times of low sea level. However, disabling that flow has only subtle impacts on the other aspects of the methane cycle on the shelf. Spikes of methane emission during late deglaciation get somewhat more intense.

4. Implications of the Model Results for the Real Siberian Continental Margin

This is the first simulation of the full methane cycle on the Siberian continental margin, or any other location with embedded permafrost soils, including hydrate formation and transient fluxes. It is internally consistent, linking processes from the ocean, the sea floor, and the deep Earth, within constraints of sediment accommodation and conservation of carbon, through geologic time. As such it has some lessons to teach us about the real Siberian continental margin. However, many of the model variables are not well known, such as the methaneogenesis rates or soil permeabilities, meaning that in some aspects the model results are not a strong constraint on reality.

The absolute values of the methane inventories in the system, as hydrate and bubbles, are not well constrained theoretically. The rate of methane production in shallow sediments is not well characterized. In reality there might be some flux of methane from the crust, but this is not included in the simulation. The transport of bubbles through the sediment column is mechanistically poorly understood, therefore not well represented in the code, which affects the inventories of bubbles in the sediment.

Ultimately the bubble concentration in the model reaches a rough steady state where production of methane gas balances its escape through the sediment column, but the steady state value from the model could be wrong. The model lacks faults, permeable layers, or the ability to "blow out", producing the sedimentary wipe-out zones observed seismically in the subsurface [*Riedel et al.*, 2002], and the pockmarks at the sediment surface [*Hill et al.*, 2004]. On land, the model lacks seasonal melting of surface permafrost (to form the active layer) and the thaw bulbs underneath lakes and rivers. In the ocean, the intensity of water column dissolution of rising bubbles depends on the bubble sizes, which depend on the gas emission rate, ultimately driven by details of gas transport in the sediment, which are neglected in the model.

These uncertainties all affect the flux of methane to the atmosphere, which is therefore not well constrained by the model. However, the model is consistent with observations [*Kort et al.*, 2012], that the total atmospheric methane flux from the Siberian margin is a small fraction of the global flux of methane to the atmosphere, and thus represents only a minor climate forcing. The model would have to be pushed very hard (as would the measurements) to fundamentally change this conclusion.

The model bubble flux to the atmosphere in the base case in analog present-day conditions is only 0.02 Tg CH_4 per year, which is an order of magnitude lower than an estimate of the total methane emission rate from aircraft [*Kort et al.*, 2012] of 0.3 Tg CH_4 / yr. However, the model only accounts (crudely) for the bubble flux to the atmosphere, and does not include gas exchange evasion of methane from the water column, which could be significant. Concentrations of methane in the water column of 50 nM are common [*Shakhova et al.*, 2010a], which, if they were unimpeded by sea ice, could lead to a flux from the region of 0.4 Tg CH_4 / yr (assuming a typical gas exchange piston velocity of 3 m/day). Methane fluxes into the water column range up to 0.4 Tg CH_4 / yr during times of relatively high sea level. Once released to the water column, the fate of a methane molecule will depend on its lifetime with respect to oxidation, which could be up to a year in the open water column [*Valentine et al.*, 2001], versus its lifetime with respect to gas exchange, which for ice-unimpeded conditions would be just a few months for a 50-meter deep water column. Thus the methane in bubbles dissolving in the water column has some chance of making it to the atmosphere anyway, depending on stratification in the water column and the extent of ice, and the gas exchange flux has the potential to be significant in the regional total flux.

Shakhova et al [2010b] proposed that 50 Gton C as methane could erupt from the Arctic on a time scale of a few years. As has been acknowledged, the model provides poor constraint on the standing stock of bubbles or methane hydrate in the sediment column, and neglects many of the mechanisms that could come into play in transporting methane quickly to the atmosphere, such as faults, channels, and blowouts of the sediment column. However, one seemingly robust model result is the thermodynamic exclusion of methane hydrate from the permafrost zone, by competition for water between ice and hydrate. Thermodynamics does not control everything, especially at low temperature, but kinetic inhibitions are more often found for nucleation steps rather than decomposition. To find an accumulation of “metastable” hydrate would also require some sort of transport mechanism of hydrate into the region where it is unstable, which does not exist. There is no reason to imagine that hydrate could form in situ when thermodynamic conditions are wrong for it. A kinetic inhibition of water-ice formation would work, but ice does not tend to super-cool in a dirty, nucleation-site-rich environment like sediments. Therefore it seems as though methane hydrate should not be expected in sediment depths shallower than about 300 meters. A warming perturbation at the sea floor today will not reach this depth for hundreds or thousands of years.

Could an abrupt methane release arise from release of trapped bubbles from melting ice? The model actually does produce a glacial cycle in bubble inventory, with changes exceeding 50 Gton over a cycle, apparently driven by methane exclusion from ice formation (Figure 15). But the model does not deliver an abrupt release in response to anthropogenic warming for any of its sensitivity studies (Figure 18). Permafrost melting driven by deglacial sea level rise has already been going on for thousands of years. In this span of time a temperature anomaly has diffused quite deep into the sediment column. In order for the abrupt temperature anomaly of global warming to further accelerate the ongoing ice or hydrate melting, it will have to diffuse down in the sediment column to where the ice still is. We would get a faster initial response to global warming if the transition from glacial to global warming sediment surface temperatures hadn’t mostly happened thousands of years ago.

In the real world, geological features such as faults and permeable layers dominate the methane cycle in the sediments. A continuum model such as this one predicts a smooth methane release response to a warming, growing in on some e-folding time-scale. A world dominated by features that each represent a small fraction of the total methane reservoir will release methane more episodically, but the statistical distribution of the response in time should still show the e-folding time scale of the underlying driving mechanism, the diffusion of heat into the sediment column. The way to deliver 50 Gton of methane to the atmosphere is for it all to be released from a single geologic feature pent up by ice. But 50 Gton of C represents a large fraction of all the traditional natural gas deposits on Earth (about 100 Gton C). The place to look for such a large unstable gas reservoir is in the field, not in this model, but until such a thing is found it remains conjecture.

Another probably robust feature of the model is the dominant impact of sea level inundation of the sediment column on the atmospheric methane flux. The methane flux is highest during cold times, because sea level is low, rather than providing a positive climate feedback of releasing methane during warm (high sea level) intervals. There is a warming positive feedback in the simulated future from climate warming, but it is much smaller than the impact of sea level changes in the past. The potential for future sea level change is much higher for the deep future, thousands of years from now, than the forecast for the year 2100, because it takes longer than a century for ice sheets to respond to changes in climate. The model finds that for the future, if sea level changes by tens of meters, as guided by paleoclimate reconstructions [*Archer and Brovkin*, 2008], the impact of sea level rise could overwhelm the impact of warming. The dominance of sea level over temperature in the model of this area is due to dissolution of methane in the water column, rather than a pressure effect on hydrate stability, which is generally a weaker driver than ocean temperature in deeper-water settings [*Mienert et al.*, 2005].

5. Bibliography

Archer, D., and V. Brovkin, The millennial lifetime of fossil fuel CO2, *Climatic Change*, *90*, 283-297, 2008.

Archer, D.E., B.A. Buffett, and P.C. McGuire, A two-dimensional model of the passive coastal margin deep sedimentary carbon and methane cycles, *Biogeosciences*, *9*, 1-20, 2012.

Archer, D.E., M. Eby, V. Brovkin, A.J. Ridgewell, L. Cao, U. Mikolajewicz, K. Caldeira, H. Matsueda, G. Munhoven, A. Montenegro, and K. Tokos, Atmospheric lifetime of fossil fuel carbon dioxide, *Ann. Reviews Earth Planet Sci.*, *37*, 117-34, 2009.

Cramer, B., and D. Franke, Indications for an active petroleum system in the Laptev Sea, NE Siberia, *Journal of Petroleum Geology*, *28* (4), 369-383, 2005.

Dallimore, S.R., and T.S. Collett, Intrapermafrost Gas Hydrates from a Deep Core-Hole in the Mackenzie Delta, Northwest-Territories, Canada, *Geology*, *23* (6), 527-530, 1995.

Dutta, K., E.A.G. Schuur, J.C. Neff, and S.A. Zimov, Potential carbon release from permafrost soils of Northeastern Siberia, *Global Change Biology*, *12* (12), 2336-2351, 2006.

Gavrilov, A.V., X.N. Romanovskii, V.E. Romanovsky, H.W. Hubberten, and V.E. Tumskoy, Reconstruction of ice complex remnants on the eastern Siberian Arctic Shelf, *Permafrost and Periglacial Processes*, *14* (2), 187-198, 2003.

Gentz, T., E. Damm, J.S. von Deimling, S. Mau, D.F. McGinnis, and M. Schluter, A water column study of methane around gas flares located at the West Spitsbergen continental margin, *Continental Shelf Research*, *72*, 107-118, 2014.

Gilichinsky, D., E. Rivkina, C. Bakermans, V. Shcherbakova, L. Petrovskaya, S. Ozerskaya, N. Ivanushkina, G. Kochkina, K. Laurinavichuis, S. Pecheritsina, R. Fattakhova, and J.M. Tiedje, Biodiversity of cryopegs in permafrost, *Fems Microbiology Ecology*, *53* (1), 117-128, 2005.

Hill, J.C., N.W. Driscoll, J.K. Weissel, and J.A. Goff, Large-scale elongated gas blowouts along the US Atlantic margin, *Journal of Geophysical Research-Solid Earth*, *109* (B9), 2004.

Hunt, J.M., *Petroleum Geochemistry and Geology*, 743 pp., Freeman, New York, 1995.

Khvorostyanov, D.V., P. Ciais, G. Krinner, S.A. Zimov, C. Corradi, and G. Guggenberger, Vulnerability of permafrost carbon to global warming. Part II: sensitivity of permafrost carbon stock to global warming, *Tellus Series B-Chemical and Physical Meteorology*, *60* (2), 265-275, 2008a.

Khvorostyanov, D.V., G. Krinner, P. Ciais, M. Heimann, and S.A. Zimov, Vulnerability of permafrost carbon to global warming. Part I: model description and role of heat generated by organic matter decomposition, *Tellus Series B-Chemical and Physical Meteorology*, *60* (2), 250-264, 2008b.

Kooi, H., J. Groen, and A. Leijnse, Modes of seawater intrusion during transgressions, *Water Resources Res.*, *36* (12), 3581-3589, 2000.

Kort, E.A., S.C. Wofsy, B.C. Daube, M. Diao, J.W. Elkins, R.S. Gao, E.J. Hintsa, D.F. Hurst, R. Jimenez, F.L. Moore, J.R. Spackman, and M.A. Zondlo, Atmospheric observations of Arctic Ocean methane emissions up to 82 degrees north, *Nature Geoscience*, *5* (5), 318-321, 2012.

Lu, C., and A.D. Werner, Timescales of seawater intrusion and retreat, *Advances in Water Resources*, *59*, 39-51, 2013.

Martin, P.A., D.W. Lea, Y. Rosenthal, N.J. Shackleton, M. Sarnthein, and T. Papenfuss, Quaternary deep sea temperature histories derived from benthic foraminiferal Mg/Ca, *Earth and Planetary Science Letters*, *198* (1-2), 193-209, 2002.

Middelburg, J.J., K. Soetaert, and P.M.J. Herman, Empirical relations for use in global diagenetic models, *Deep-Sea Research I*, *44*, 327-344, 1997.

Mienert, J., M. Vanneste, S. Bunz, K. Andreassen, H. Haflidason, and H.P. Sejrup, Ocean warming and gas hydrate stability on the mid-Norwegian margin at the Storegga Slide, *Marine and Petroleum Geology*, *22* (1-2), 233-244, 2005.

Moore, W.S., C.A. Carlson, and S.J. Giovannoni, The Effect of Submarine Groundwater Discharge on the Ocean, *Annual Review of Marine Science*, *2*, 59-88, 2011.

Nicolsky, D., and N. Shakhova, Modeling sub-sea permafrost in the East Siberian Arctic Shelf: the Dmitry Laptev Strait, *Environmental Research Letters*, *5* (1), 2010.

Nicolsky, D.J., V.E. Romanovsky, N.N. Romanovskii, A.L. Kholodov, N.E. Shakhova, and I.P. Semiletov, Modeling sub-sea permafrost in the East Siberian Arctic Shelf: The Laptev Sea region, *Journal of Geophysical Research-Earth Surface*, *117*, 2012.

Portnov, A., A.J. Smith, J. Mienert, G. Cherkashov, P. Rekant, P. Semenov, P. Serov, and B. Vanshtein, Offshore permafrost decay and massive seabed methane escape in water depths > 20m at the South Kara Sea shelf, *Geophysical Research Letters*, *40* (15), 3962-3967, 2013.

Post, V.E.A., J. Groen, H. Kooi, M. Person, S.M. Ge, and W.M. Edmunds, Offshore fresh groundwater reserves as a global phenomenon, *Nature*, *504* (7478), 71-78, 2013.

Reagan, M.T., Dynamic response of oceanic hydrate deposits to ocean temperature change, *Journal of Geophysical Research-Oceans*, *113* (C12), 2008.

Reagan, M.T., and G.J. Moridis, Large-scale simulation of methane hydrate dissociation along the West Spitsbergen Margin, *Geophysical Research Letters*, *36*, 2009.

Reagan, M.T., G.J. Moridis, S.M. Elliott, and M. Maltrud, Contribution of oceanic gas hydrate dissociation to the formation of Arctic Ocean methane plumes, *Journal of Geophysical Research-Oceans*, *116*, 2011.

Riedel, M., G.D. Spence, N.R. Chapman, and R.D. Hyndman, Seismic investigations of a vent field associated with gas hydrates, offshore Vancouver Island, *Journal of Geophysical Research-Solid Earth*, *107* (B9), 2002.

Romanovskii, N.N., and H.W. Hubberten, Results of permafrost modelling of the lowlands and shelf of the Laptev Sea region, Russia, *Permafrost and Periglacial Processes*, *12* (2), 191-202, 2001.

Romanovskii, N.N., H.W. Hubberten, A. Gavrilov, V.E. Tumskoy, and A.L. Kholodov, Permafrost of the east Siberian Arctic shelf and coastal lowlands, *Quaternary Science Reviews*, *23* (11-13), 1359-1369, 2004.

Romanovskii, N.N., H.W. Hubberten, A.V. Gavrilov, A.A. Eliseeva, and G.S. Tipenko, Offshore permafrost and gas hydrate stability zone on the shelf of East Siberian Seas, *Geo-Marine Letters*, *25* (2-3), 167-182, 2005.

Romanovskii, N.N., H.W. Hubberten, A.V. Gavrilov, V.E. Tumskoy, G.S. Tipenko, M.N. Grigoriev, and C. Siegert, Thermokarst and land-ocean interactions, Laptev Sea Region, Russia, *Permafrost and Periglacial Processes*, *11* (2), 137-152, 2000.

Schuur, E.A.G., J. Bockheim, J.G. Canadell, E. Euskirchen, C.B. Field, S.V. Goryachkin, S. Hagemann, P. Kuhry, P.M. Lafleur, H. Lee, G. Mazhitova, F.E. Nelson, A. Rinke, V.E. Romanovsky, N. Shiklomanov, C. Tarnocai, S. Venevsky, J.G. Vogel, and S.A. Zimov, Vulnerability of permafrost carbon to climate change: Implications for the global carbon cycle, *Bioscience*, *58* (8), 701-714, 2008.

Shakhova, N., Geochemical and geophysical evidence of methane release over the East Siberian Arctic Shelf, *Journal of Geophysical Research-Oceans*, *115*, 10.1029/2009JC005602, 2010.

Shakhova, N., I. Semiletov, and G. Panteleev, The distribution of methane on the Siberian Arctic shelves: Implications for the marine methane cycle, *Geophysical Research Letters*, *32* (9), 2005.

Shakhova, N., I. Semiletov, A. Salyuk, V. Yusupov, D. Kosmach, and O. Gustafsson, Extensive Methane Venting to the Atmosphere from Sediments of the East Siberian Arctic Shelf, *Science*, *327* (5970), 1246-1250, 2010a.

Shakhova, N.E., V.A. Alekseev, and I.P. Semiletov, Predicted methane emission on the East Siberian shelf, *Doklady Earth Sciences*, *430* (2), 190-193, 2010b.

Shakhova, N.E., D.Y. Nicolsky, and I.P. Semiletov, Current state of subsea permafrost on the East Siberian Shelf: Tests of modeling results based on field observations, *Doklady Earth Sciences*, *429* (2), 1518-1521, 2009.

Stein, R., and K. Fahl, Holocene accumulation of organic carbon at the Laptev Sea continental margin (Arctic Ocean): sources, pathways, and sinks, *Geo-Marine Letters*, *20* (1), 27-36, 2000.

Stouffer, R.J., and S. Manabe, Equilibrium response of thermohaline circulation to large changes in atmospheric CO2 concentration, *Clim. Dynamics*, *20*, 759-773, 2003.

Taylor, A.E., S.R. Dallimore, and S.I. Outcalt, Late quaternary history of the Mackenzie-Beaufort region, Arctic Canada, from modelling of permafrost temperatures .1. The onshore offshore transition, *Canadian Journal of Earth Sciences*, *33* (1), 52-61, 1996.

Valentine, D.L., D.C. Blanton, W.S. Reeburgh, and M. Kastner, Water column methane oxidation adjacent to an area of active hydrate dissociation, Eel River Basin, *Geochimica Et Cosmochimica Acta*, *65* (16), 2633-2640, 2001.

Verrjuit, A., A note on the Ghyben-Herzberg formula, *Bull. Int. Assoc. Sci. Hydrology*, *13* (4), 43-46, 1968.

Walter, K.M., S.A. Zimov, J.P. Chanton, D. Verbyla, and F.S. Chapin, Methane bubbling from Siberian thaw lakes as a positive feedback to climate warming, *Nature*, *443* (7107), 71-75, 2006.

Watson, T.A., A.D. Werner, and C.T. Simmons, Transience of seawater intrusion in response to sea level rise, *Water Resources Res.*, *40* (W12533), doi:10.1029/2010WR009564, 2010.

Westbrook, G.K., Escape of methane gas from the seabed along the West Spitsbergen, *Geophysical Research Letters*, *36*, 2009.

Westbrook, G.K., K.E. Thatcher, E.J. Rohling, A.M. Piotrowski, H. Paelike, A.H. Osborne, E.G. Nisbet, T.A. Minshull, M. Lanoiselle, R.H. James, V. Huehnerbach, D. Green, R.E. Fisher, A.J. Crocker, A. Chabert, C. Bolton, A. Beszczynska-Moeller, C. Berndt, and A. Aquilina, Escape of methane gas from the seabed along the West Spitsbergen continental margin, *Geophysical Research Letters*, *36*, 2009.

Zimov, S.A., S.P. Davydov, G.M. Zimova, A.I. Davydova, E.A.G. Schuur, K. Dutta, and F.S. Chapin, III, Permafrost carbon: Stock and decomposability of a globally significant carbon pool, *Geophysical Research Letters*, *33* (20), 2006.

6. Figure Captions

Figure 1. Thermodynamics of hydrate and ice. Top) Colors are salinities, which range from fresh if there is no solid phase, to saltier as the freezing point depression of the solid phase follows the in situ temperature. Contours indicate the extent of thermal disequilbrium, $\Delta T_{eq} = T - T_{eq}$. a) For the system of ice and fluid. b) Considering hydrate and fluid phases, excluding ice formation and assuming equilibrium with methane gas. c) Combined ice + hydrate + fluid system, where the salinity is controlled by the most stable solid phase. Solid contours are $\Delta T_{eq,\ hydrate}$, dashed $\Delta T_{eq,\ ice}$. d and e) Colors are ΔT_{eq}, where 0 (purple) indicates stability, and contours are the excess salinity relative to a solid phase, e.g. S_{max} - $S_{eq,\ hydrate}$ in (d), for hydrate, and e) ice. f) Phase diagram for the ice + hydrate + brine system. Hydrate is excluded from the ice phase space by the high salinity of the brine. Ice is ideally also excluded from part of the hydrate stability zone by a similar mechanism, but this would only happen in nature under conditions of unlimited methane availability. Thus it is easier to envision coexistence of hydrate and ice within the hydrate stability zone, under conditions of limited methane availability, than it is to imagine hydrate in the permafrost zone, where ice has no impediment for formation.

Figure 2. Domain of the model as applied to the Laptev Sea continental shelf and slope. This is the result of 62 million years of sediment accumulation on the crust, isostatic subsidence, pore fluid flow, and thermal diffusion, used as the initial condition for glacial / interglacial cycle and climate change simulations. Color indicates temperature. a) Full view. Black line shows the bottom of the crust, which grades smoothly from continental on the left into ocean crust through most of the domain on the right. b) Zoom in to see increased model resolution in the upper kilometer of the sediment column.

Figure 3. Particulate Organic Carbon (POC) concentration. Highest values are found in the sediment depocenter just off the continental shelf break.

Figure 4. Pore water salinity a) The fully marine case, in which the sediment column has always been submerged underneath a time-invariant sea level. b) Result of sediment column freshening by hydrological groundwater flow, driven by the pressure head resulting from a water table higher than sea level. A movie of the transition from marine to

freshened (the origin of b) can be seen at http://geosci.uchicago.edu/~archer/spongebob_arctic/fig4.movie.gif

Figure 5. Initial distribution of dissolved methane. a) Concentration in moles/m^3. b-d) $\Omega = CH_4 / CH_{4(sat)}$ deviation from equilibrium, b) of the Marine (salty) initial condition; c) of the pre-freshened initial condition (note depletion in near-surface near-shore sediments in the upper left); d) including permeable channels every five grid points, plus pre-freshening.

Figure 6. Freshening the sediment column by hydrological groundwater flushing. Color indicates salinity. Solid black line represents sea level in the ocean (white space), and the equilibrium fresh-salty boundary given a snapshot of the pressure head (the Ghyben-Herzberg relation). Left side: results of dropping sea level 30 meters and holding it there. A freshwater lens forms and strives to reach Ghyben Herzberg equilibrium as the sediment column subsides, where atmospheric exposure decreases its buoyancy and stops sediment accumulation. After the sediment column subsides beneath the still-lowered sea level, the fresh water lens remains for millions of years. A movie can be seen at http://geosci.uchicago.edu/~archer/spongebob_arctic/fig6a.movie.gif . Right side: Result of dropping sea level 120 meters and holding it there forever. Movie at http://geosci.uchicago.edu/~archer/spongebob_arctic/fig6b.movie.gif

Figure 7. Time scale of depleting the salinity of the continental shelf sediment column after an instantaneous sea level drop of 30 meters. The effect of lateral canyons is to provide a pathway for saline fluid to be replaced by fresh groundwater in sediments above sea level. If the lateral canyon spacing is 10 km, they can have a significant impact on the time constant for ground water flushing. A more conservative 100-km canyon is adopted for the rest of the simulations.

Figure 8. Dissolved methane impact by hydrological freshening of the sediment column as described in Figure 5. $\Omega = CH_4 / CH_{4(sat)}$. Movies can be seen at http://geosci.uchicago.edu/~archer/spongebob_arctic/fig8a.movie.gif and http://geosci.uchicago.edu/~archer/spongebob_arctic/fig8b.movie.gif

Figure 9. Time-dependent forcing for the glacial / interglacial simulations and the global warming scenarios. a) Sea level is imposed as a sawtooth 100-kyr cycle, with interglacial intervals shaded. The GW+S simulation tracks potential changes in sea level on long time scales due to fossil fuel CO_2 release, following a covariation from the geologic past of 15 meters / °C. The GW and Control simulations hold sea level at interglacial levels. b) Ocean temperature forcings.

Figure 10. Colors indicate salinity in the unfrozen pore fluid of the sediment column. Thin solid black contours show the frozen fraction of the pore space. Heavy black stippled contour shows the stability boundary of methane hydrate as a function of temperature, pressure, and unfrozen pore fluid salinity. Left side: previously pre-freshened initial condition. Right side: Pure marine initial condition. c-d) Lowered sea level (from 70 kyr in Figure 8) but warm air temperatures prevent permafrost formation. e-f) Glacial conditions of lowered sea level (70 kyr) and atmospheric temperature of –17 °C driving permafrost formation. The pre-freshened and the marine initial conditions differ in the frozen fraction of sediment, but the salinity of the unfrozen fluid, a correlate of the activity of water, depends only the temperature. g-h) Rising sea level (at 90 kyr in Figure 8) into an interglacial interval. Movies of the glacial cycles (GL) with the prefreshened initial condition can be seen at http://geosci.uchicago.edu/~archer/spongebob_arctic/fig10a.movie.gif , and the marine initial condition at http://geosci.uchicago.edu/~archer/spongebob_arctic/fig10b.movie.gif.

Figure 11. Pore fluid pressure forcing and flow through the glacial cycles. Left) Colors indicate $P_{excess} + P_{head}$, solid contours are ice fraction, dashed contours are P_{head}. Right) Colors indicate $P_{excess} + P_{head}$, note different color scale from Left. Initial refers to the prefreshened initial condition. "Low Sea Level" refers to simulation SL. "Glacial" and "Interglacial" refer to simulation GL. Dashed contours indicate ice fraction, vectors fluid velocity. Movies of the prefreshened initial condition and glacial cycles (GL) can be seen at http://geosci.uchicago.edu/~archer/spongebob_arctic/press_uw.65e6.nc.ld2.gl.pf_eq.gw.comp.movie.gif and http://geosci.uchicago.edu/~archer/spongebob_arctic/pressure_flow.65e6.nc.ld2.gl.pf_eq.gw.comp.movie.gif.

Figure 12. Sensitivities of the hydrate stability zone. Impact of the competition between ice and hydrate phases (a-d), and the geothermal

temperature gradient (e-f). When ice is included as a potential solid phase, the pore waters are salty in the permafrost zone (a), restricting hydrate stability to at least 300 meters below sea level thoughout the simulation (c). When ice is forbidden to form, hydrate can be stable nearly to the sediment surface during the height of the glaciation (b and d). The base of the stability zone is sensitive to the geothermal temperature gradient, while the shallowest reach of the stability zone does not respond to changing heat fluxes, because the temperatures are "anchored" at the ocean value at the top of the sediment column.

Figure 13. Dissolved methane concentration relative to equilibrium ($\Omega = CH_4 / CH_{4(sat)}$). Solid contours indicate ice fraction, dashed contours show the methane hydrate stability boundary. Movies for the left, center, and right columns, respectively can be seen at http://geosci.uchicago.edu/~archer/spongebob_arctic/fig13a.movie.gif , http://geosci.uchicago.edu/~archer/spongebob_arctic/fig13b.movie.gif , and http://geosci.uchicago.edu/~archer/spongebob_arctic/fig13c.movie.gif.

Figure 14. Carbon cycle through glacial cycles from a prefreshened initial condition. Solid contours: Ice Fraction. Dashed contours: Methane hydrate stability zone. Left) Particulate organic carbon (POC) concentration. Movie at http://geosci.uchicago.edu/~archer/spongebob_arctic/fig14a.movie.gif. Center) Biological methane production rate. Movie at http://geosci.uchicago.edu/~archer/spongebob_arctic/fig14b.movie.gif Right) Methane hydrate concentration. Movie at http://geosci.uchicago.edu/~archer/spongebob_arctic/fig14c.movie.gif. Movies of methane hydrate stability and concentration are given for the sensitivity studies, in the supplemental material and at http://geosci.uchicago.edu/~archer/spongebob/.

Figure 15. Glacial cycle of methane hydrate inventory on the continental shelf. a) Effects of salt and ice. b) Sensitivity to methaneogenesis rates. c) Sensitivity to the column temperature gradient. d) Glacial cycles of shelf bubble inventories, effects of salt and ice.

Figure 16. Spatial distribution and sea level impact of methane fluxes to the atmosphere. a-d) Solid line shows the elevation of the sediment surface relative to the sea level at the time. Grey lines (scale to right)

show the efficiency of bubble transport through the water column, assuming a flux attenuation length scale of 30 meters. e-k) Dashed line: Methane bubble flux across the sediment surface. Solid line: Methane bubble flux to the atmosphere (dashed line multiplied by transport efficiency). Most of the methane flux in the model occurs near the shelf break, and submergence in the ocean has a strong impact on the flux to the atmosphere. A related movie can be seen at http://geosci.uchicago.edu/~archer/spongebob_arctic/fig16.movie.gif .

Figure 17. Glacial / interglacial cycle of methane fluxes on the continental margin of the model. Sea level at top, grey regions indicate interglacial intervals, pink the Anthropocene. a-e) Cumulative methane fluxes. Red lines show production rate. Brown regions show lateral transport of dissolved methane. Grey shows oxidation by SO_4^{2-} in the sediment column. Blue shows bubble flux to the water column. During interglacial times (e.g. far left) there is a small onshore transport of methane, which is represented by a negative starting point for the oxidation (grey) region. In equilibrium, the colored areas should fill in the region under the red curve.

Figure 18. Methane fluxes to the atmosphere. Sea level at the top, interglacial intervals in vertical grey bars, the Anthropocene in pink. a) From a pre-freshened initial condition, with and without permafrost formation. b) From a pure marine initial condition. c and d) Sensitivity to terrestrial organic carbon deposition during low sea-level stands, and to thermogenic methane flux. e) Sensitivity to the impact of ice fraction on bubble mobility.

Figure 19. Impact of anthropogenic warming on the methane cycle in the model. a) Base cases, a warming scenario (GW), without and with a geological time-scale sea level rise scenario (+SLR), and extended interglacial control (Ctl). Warming plus increasing sea level decreases the methane flux overall, due to bubble dissolution in a deeper water column. b) Altered model physics impacts. c and d) Altered methanogenesis rates. e) Sensitivity to the ice fraction at which bubble mobility is assumed stopped.

Tables

Table 1. Summary of model runs.

SL	Sea level changes with constant air and water temperatures
GL	SL + glacial cycles in air and water temperature
GW	A long-term global warming scenario, a peak and long tail temperature perturbation consistent with CO_2 release and cessation of the glacial sawtooth forcing.
+SLR	Adds geologic-timescale sea level rise due to anthropogenic climate change, based on correlation between temperature and sea level in the geologic past (10 meters / °C).
Ctl	An extended interglacial with no CO_2 release forcing.
+ LD	Land deposition of carbon-rich Yedoma. Base case is 10 m / 100 kyr, with sensitivity runs using 30 and 100 m / 100 kyr accumulation of 30% POC material. Movies in the supplemental material are identified by the tags Land30 and Land100.
+ TG	Thermogenic methane production rate sensitivity runs, scaling the rate from the spinup result by factors of 10 and 100. Movies in the supplemental material are identified by the tags TGenX10 and TGenX100.
+ Geotherm	Sensitivity of ice and hydrate cycles on the geothermal temperature gradient. Temperatures from the Base simulation were adjusted when calculating the stability of ice and hydrate, to simulate the impact of

	geothermal heat fluxes on hydrate stability. Note that other aspects of the sediment column, including the solubility of methane, retained the original temperatures. Heat fluxes simulated include 25 mW/m2, 37.5, 50 (Base), 62.5, and 75. Movies of the non-base runs are identified by tags HF050, HF075, HF125, and HF150.
Ice and Bubble Transport	When the ice fraction exceeds a threshold value methane gas flow is disabled. Base case is 50%, variants 10%, 30%, 70%, and 90%, identified with tags Ice10, Ice30, Ice70, and Ice90.
No Ice	The ice phase is disallowed in the thermodynamic calculation. Movies in the supplemental material include salinity. The files are tagged as NoIce
No Salt from Ice	Ice is allowed to form, but it does not affect the salinity as it determines methane hydrate stability. Movie files are tagged as NoSalFromIce.
Permeable Channels	Increasing vertical permeability by a factor of 10 every 5th grid cell, to generate heterogeneity in the flow. Tagged as PermChan
No Horizontal Flow	Horizontal flow is disabled. Tagged as NoHFlow.

Movies comparing altered scenario runs with the Base scenario are given in the supplemental material, and at http://geosci.uchicago.edu/~archer/spongebob/. Movies named hydrate* and bubbles* show methane hydrate and bubble inventories and stability zone changes. Files entitled salinity* show salinities, and bubb_atm* show bubble fluxes through and out of the sediment column, into the ocean, and into the atmosphere, through time.

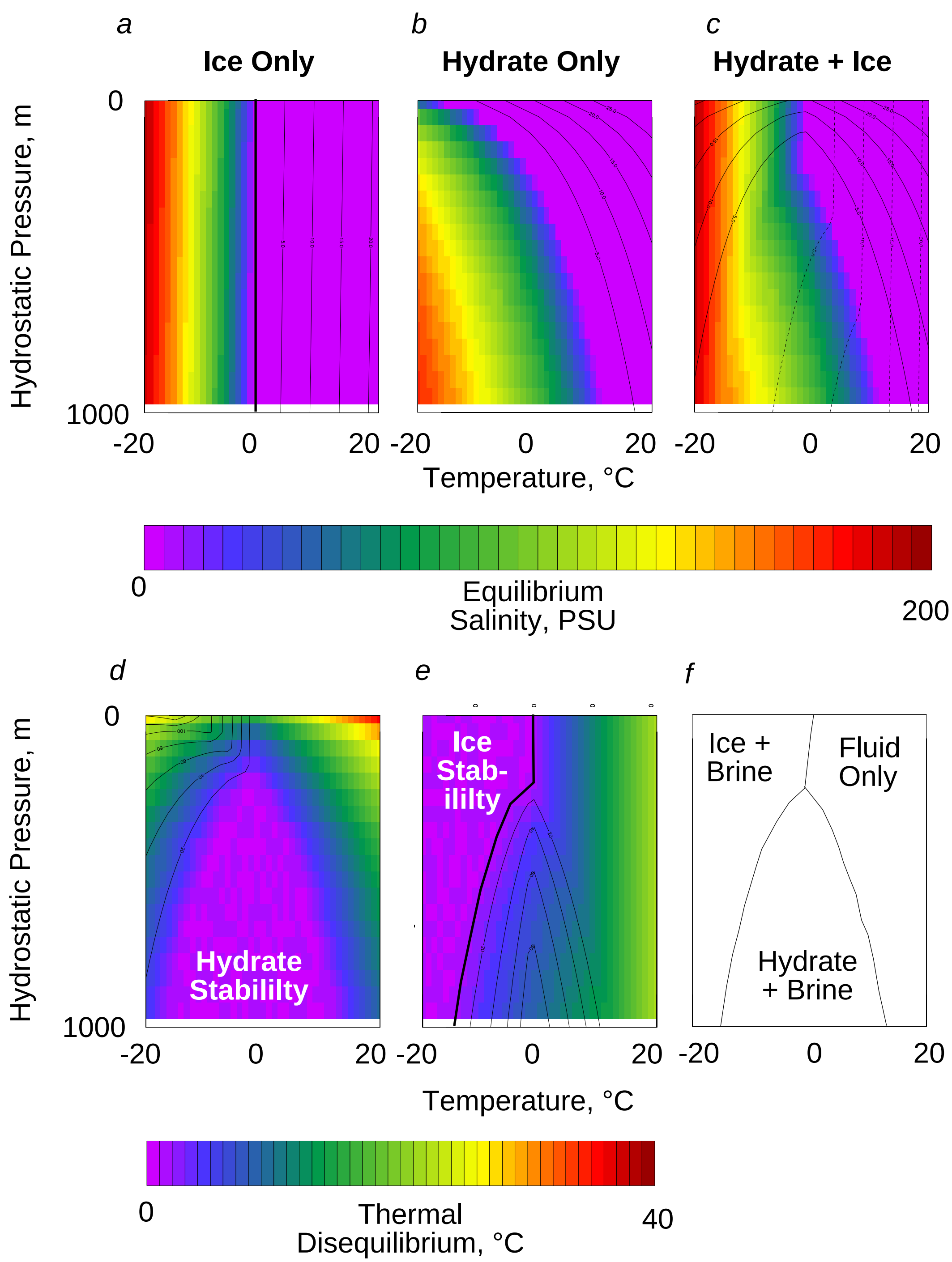
a
Ice Only
b
Hydrate Only
c
Hydrate + Ice
Hydrostatic Pressure, m
0
1000
-20
0
20
-20
0
20
-20
0
20
Temperature, °C
0
Equilibrium
Salinity, PSU
200
d
e
f
Hydrate
Stabililty
Ice
Stab-
ililty
Ice +
Brine
Fluid
Only
Hydrate
+ Brine
Hydrostatic Pressure, m
0
1000
-20
0
20
-20
0
20
-20
0
20
Temperature, °C
0
Thermal
Disequilibrium, °C
40

Figure 1

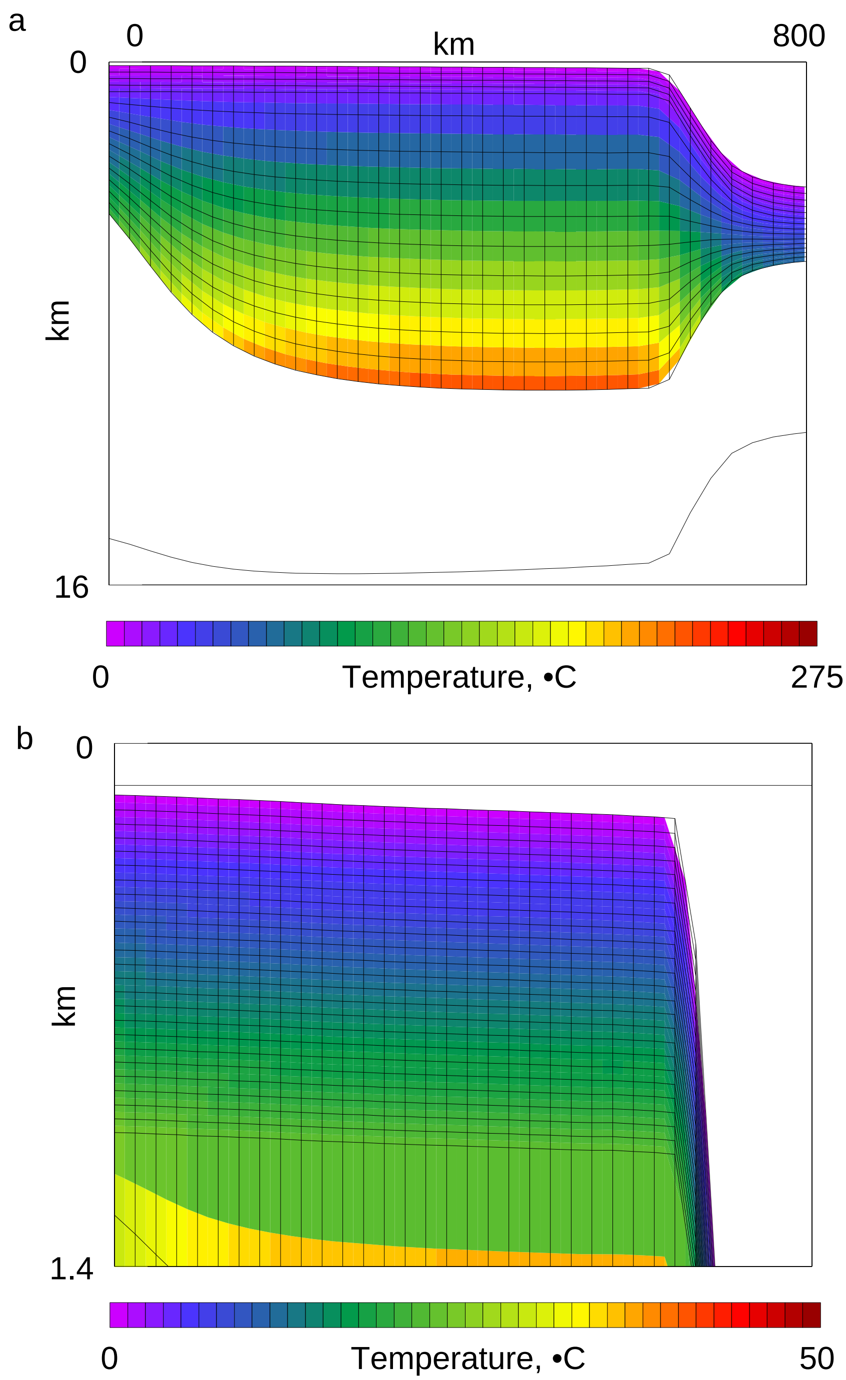

Figure 2

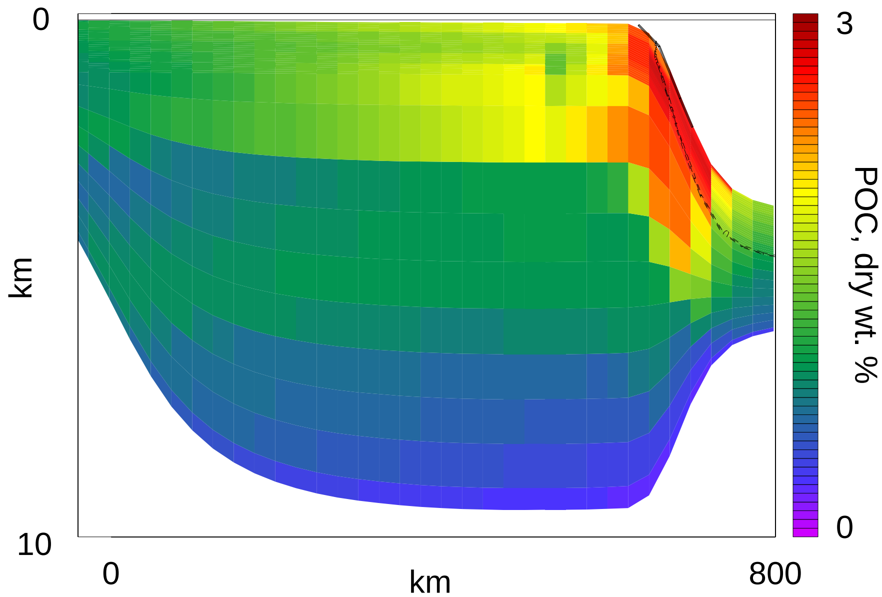

Figure 3

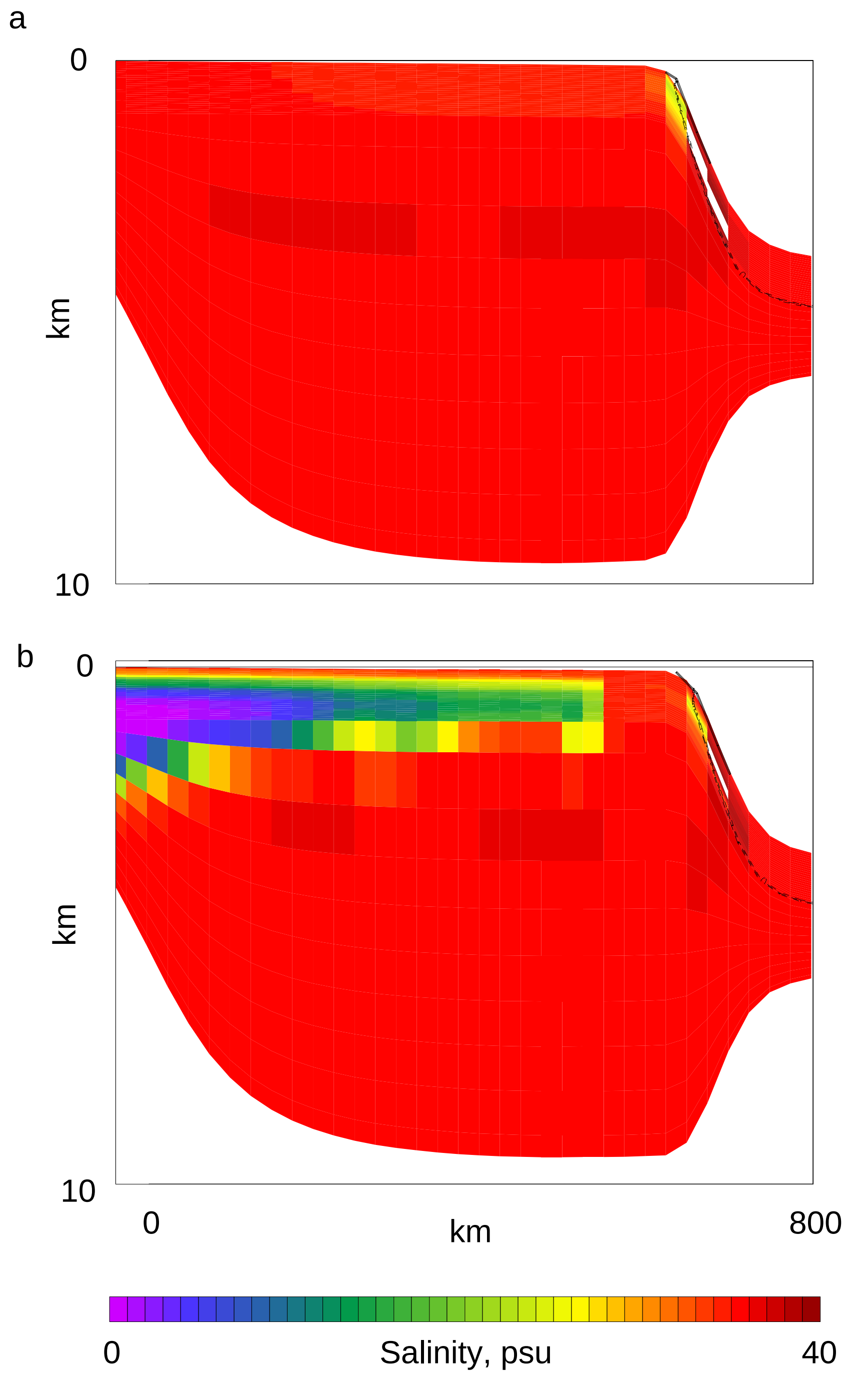

Figure 4

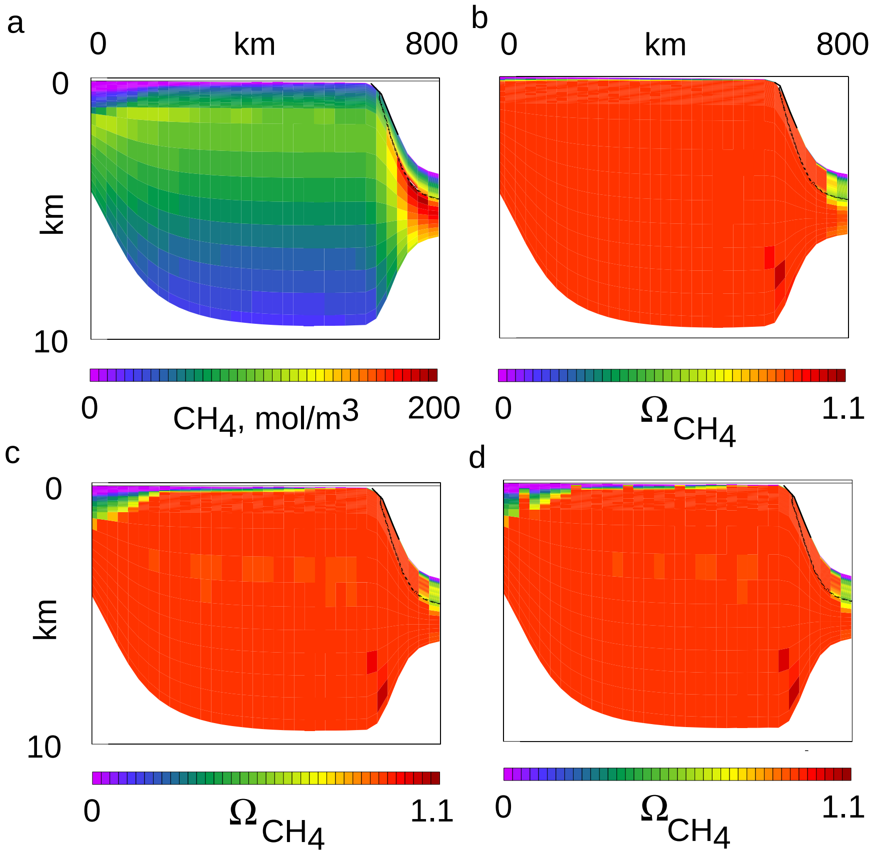
a
0
km
800
0
km
10
0
CH4, mol/m3
200
b
0
km
800
0
Ω CH4
1.1
c
0
km
10
0
Ω CH4
1.1
d
0
Ω CH4
1.1

Figure 5

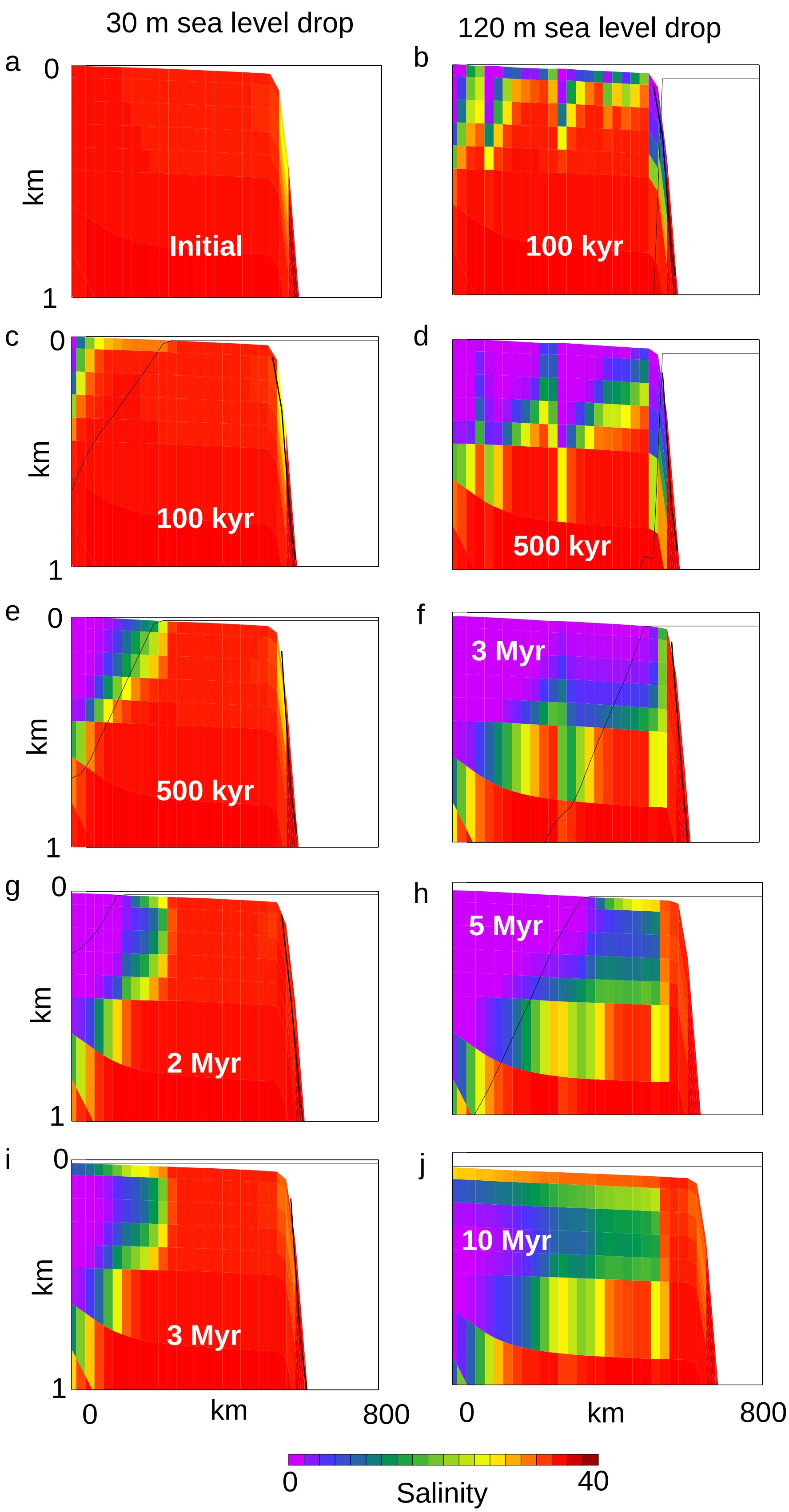
30 m sea level drop
120 m sea level drop
a
b
c
d
e
f
g
h
i
j
0
1
km
Initial
100 kyr
500 kyr
2 Myr
3 Myr
5 Myr
10 Myr
800
0
40
Salinity

Figure 6

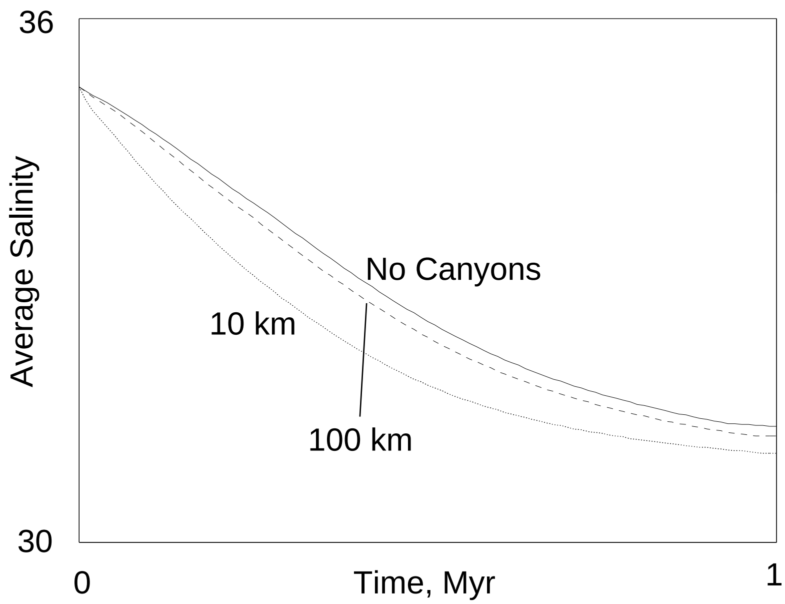

Figure 7

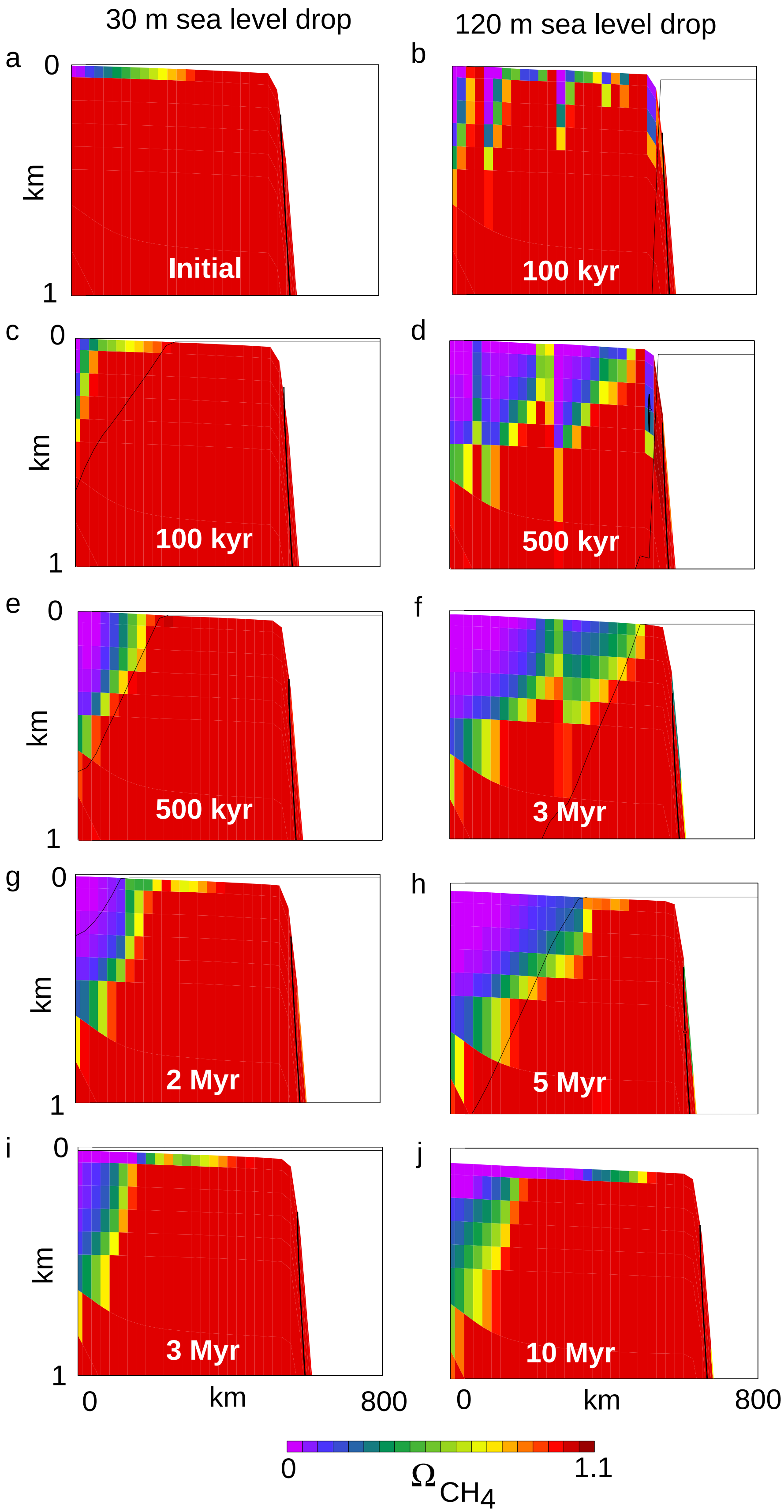
30 m sea level drop
120 m sea level drop
a
b
c
d
e
f
g
h
i
j
km
0
1
Initial
100 kyr
100 kyr
500 kyr
500 kyr
3 Myr
2 Myr
5 Myr
3 Myr
10 Myr
0
km
800
0
km
800
0
1.1
Ω_{CH_4}

Figure 8

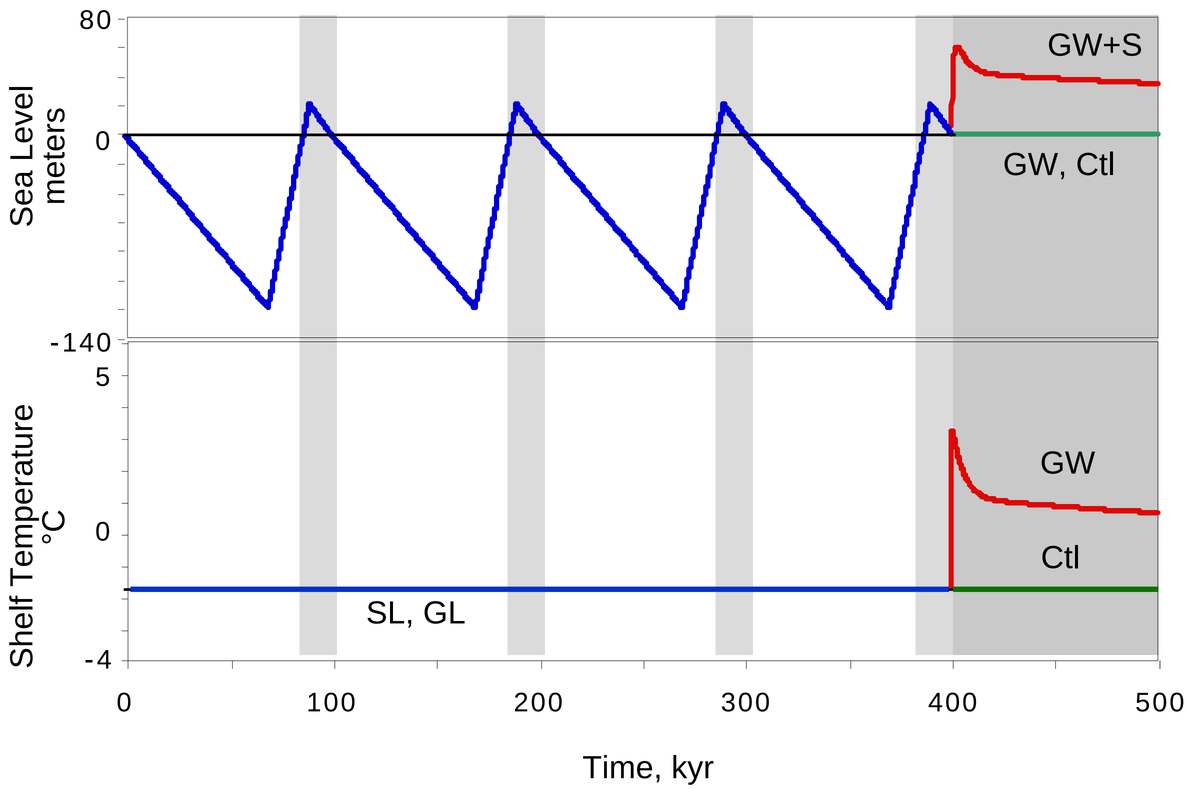
80
0
-140
Sea Level
meters
GW+S
GW, Ctl
5
0
-4
Shelf Temperature
°C
GW
Ctl
SL, GL
0
100
200
300
400
500
Time, kyr

Figure 9

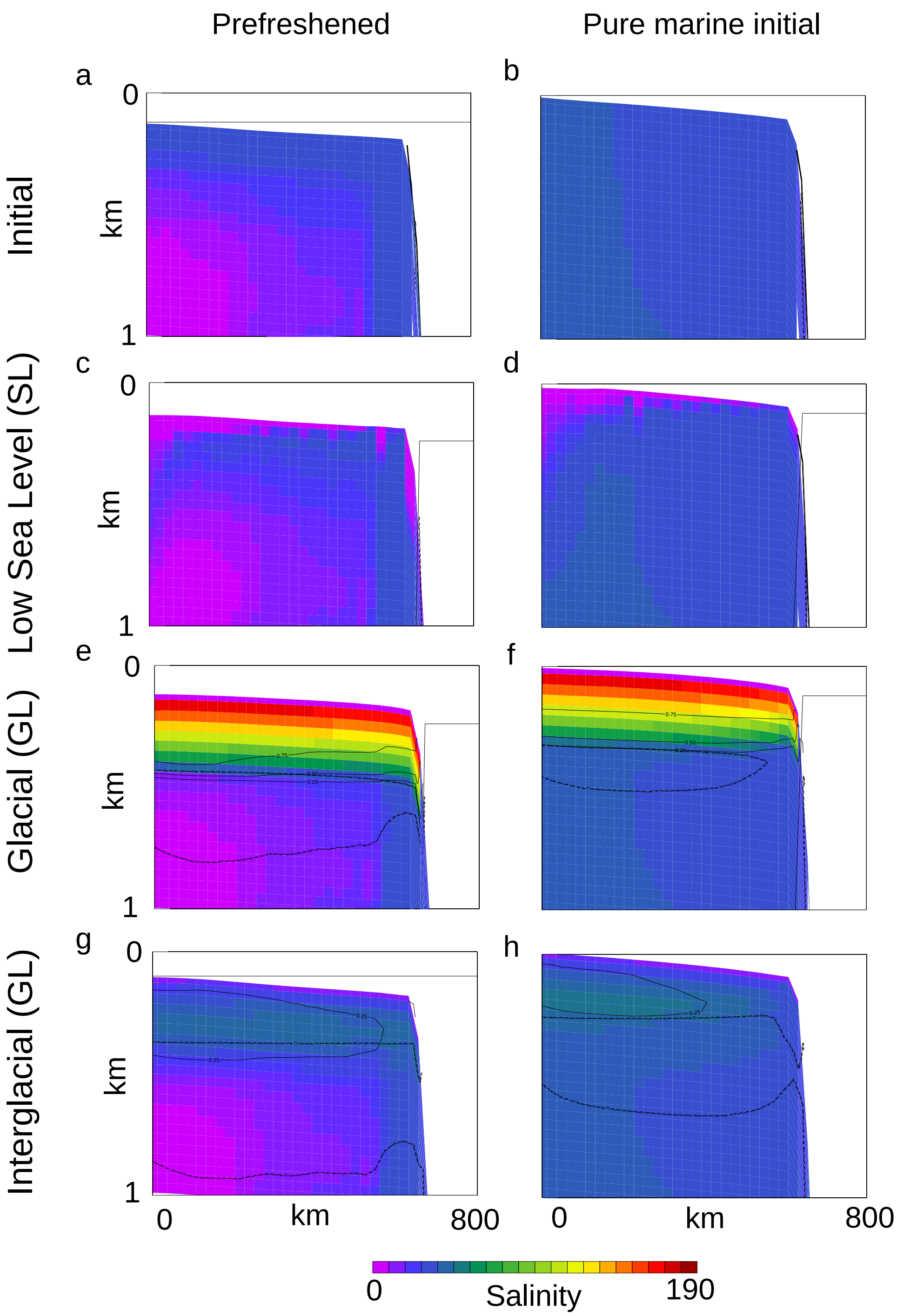

Prefreshened
Pure marine initial
a
b
c
d
e
f
g
h
Initial
Low Sea Level (SL)
Glacial (GL)
Interglacial (GL)
km
0
1
0
km
800
0
Salinity
190

Figure 10

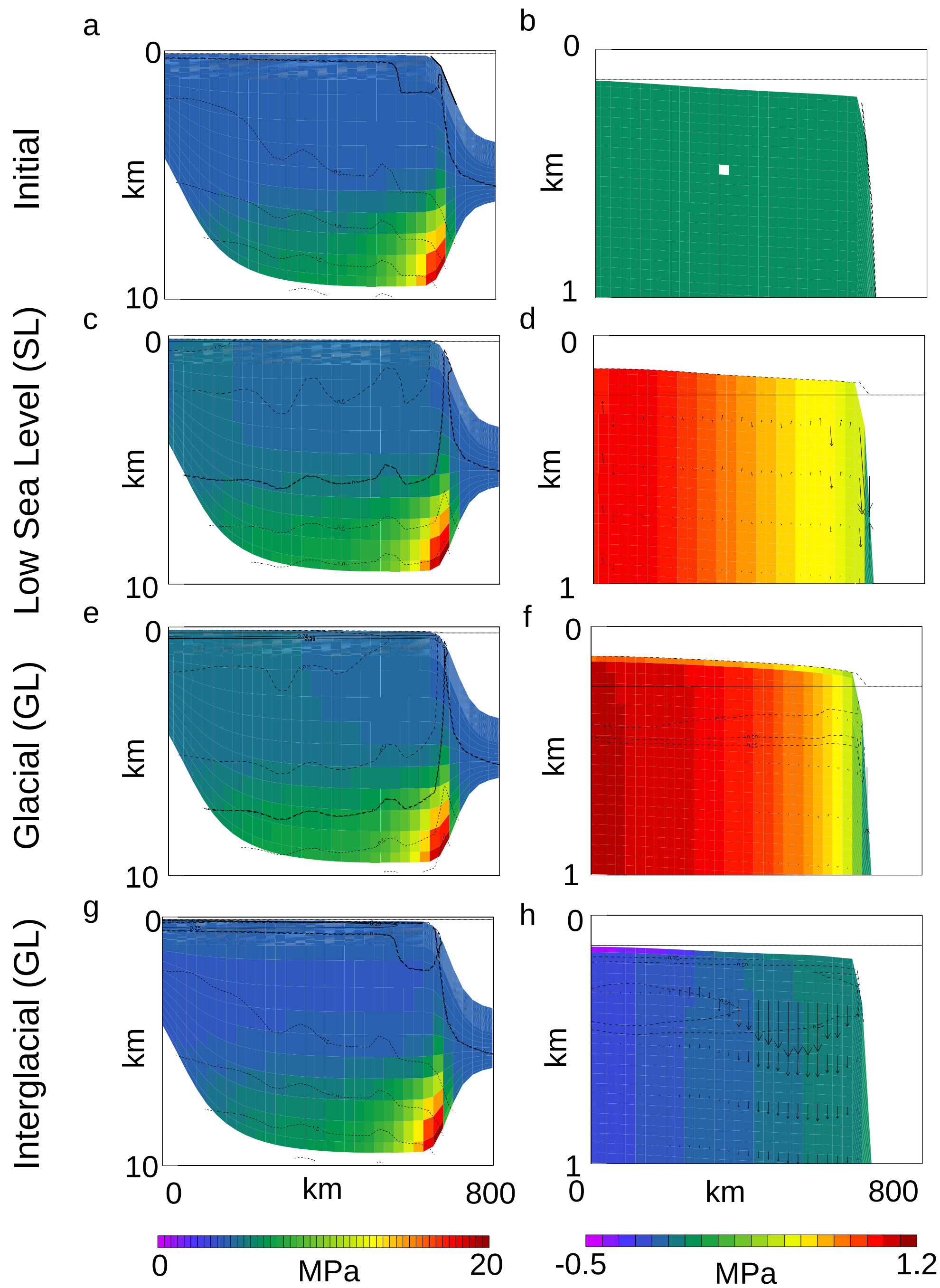
a
b
c
d
e
f
g
h
Initial
Low Sea Level (SL)
Glacial (GL)
Interglacial (GL)
km
0
10
1
800
MPa
0
20
-0.5
1.2

Figure 11

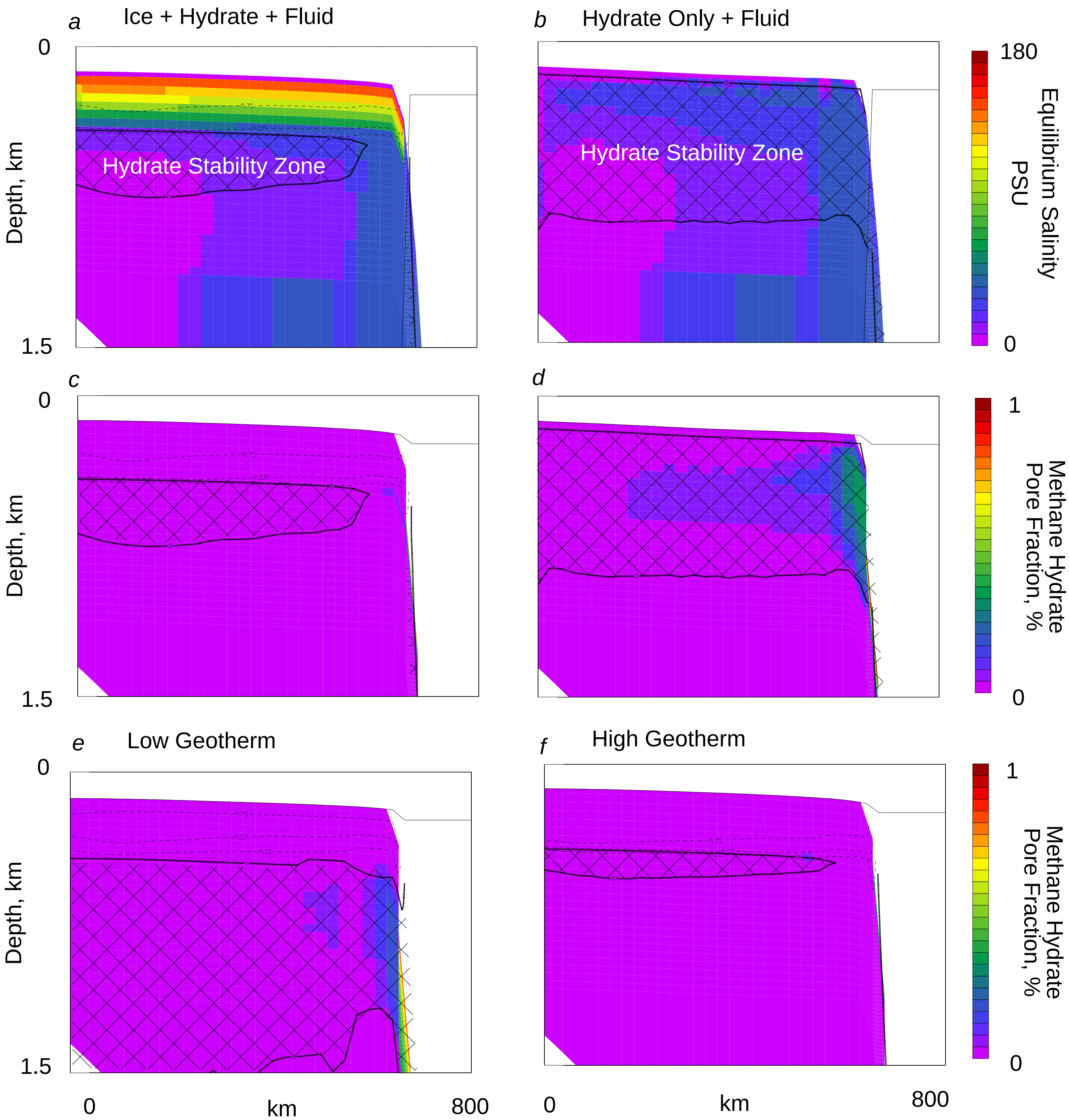

a
Ice + Hydrate + Fluid
b
Hydrate Only + Fluid
Hydrate Stability Zone
Hydrate Stability Zone
c
d
e
Low Geotherm
f
High Geotherm
Depth, km
0
1.5
km
800
180
Equilibrium Salinity
PSU
1
Methane Hydrate
Pore Fraction, %

Figure 12

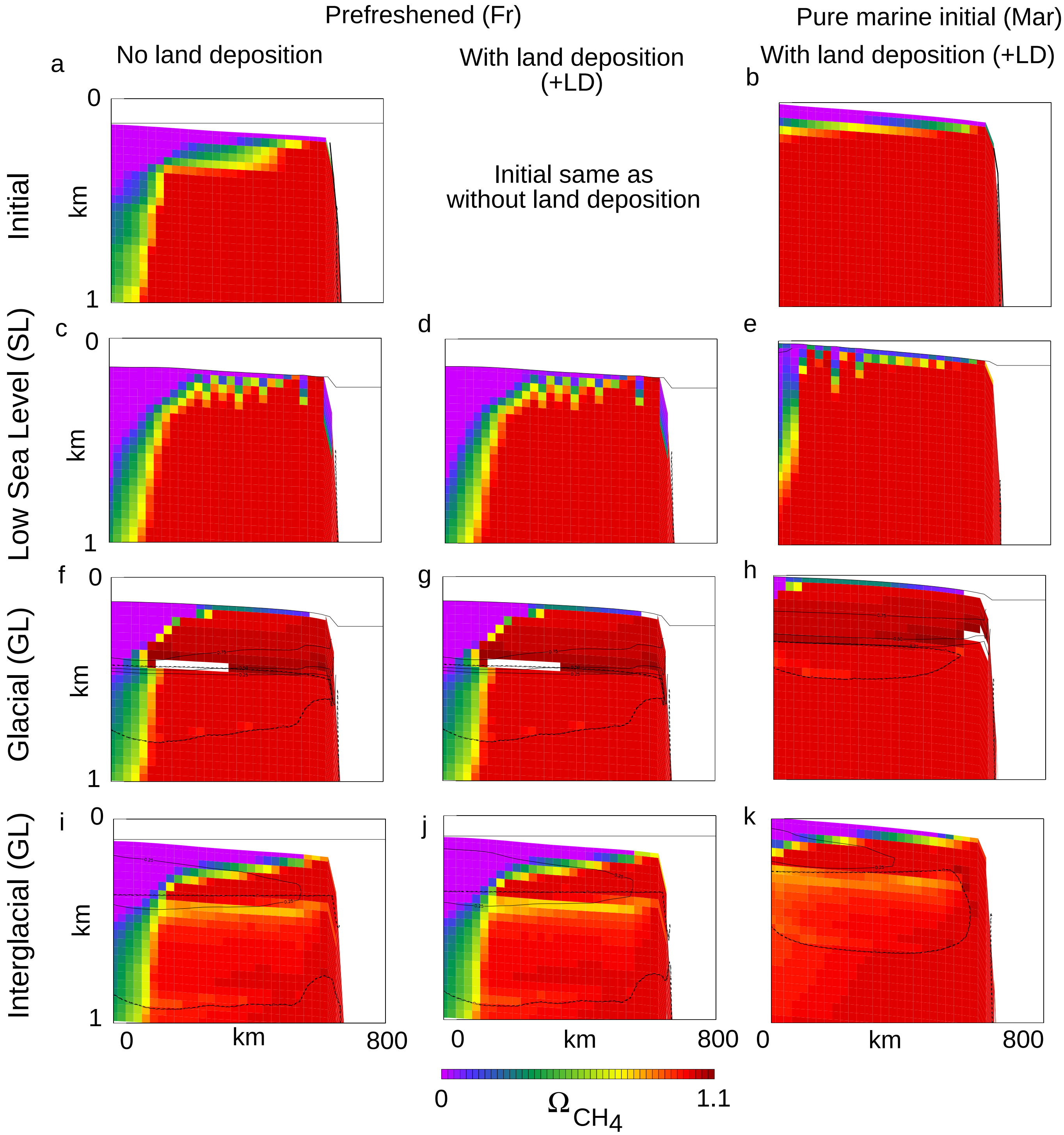

CH4 / CH4(eq)

Figure 13

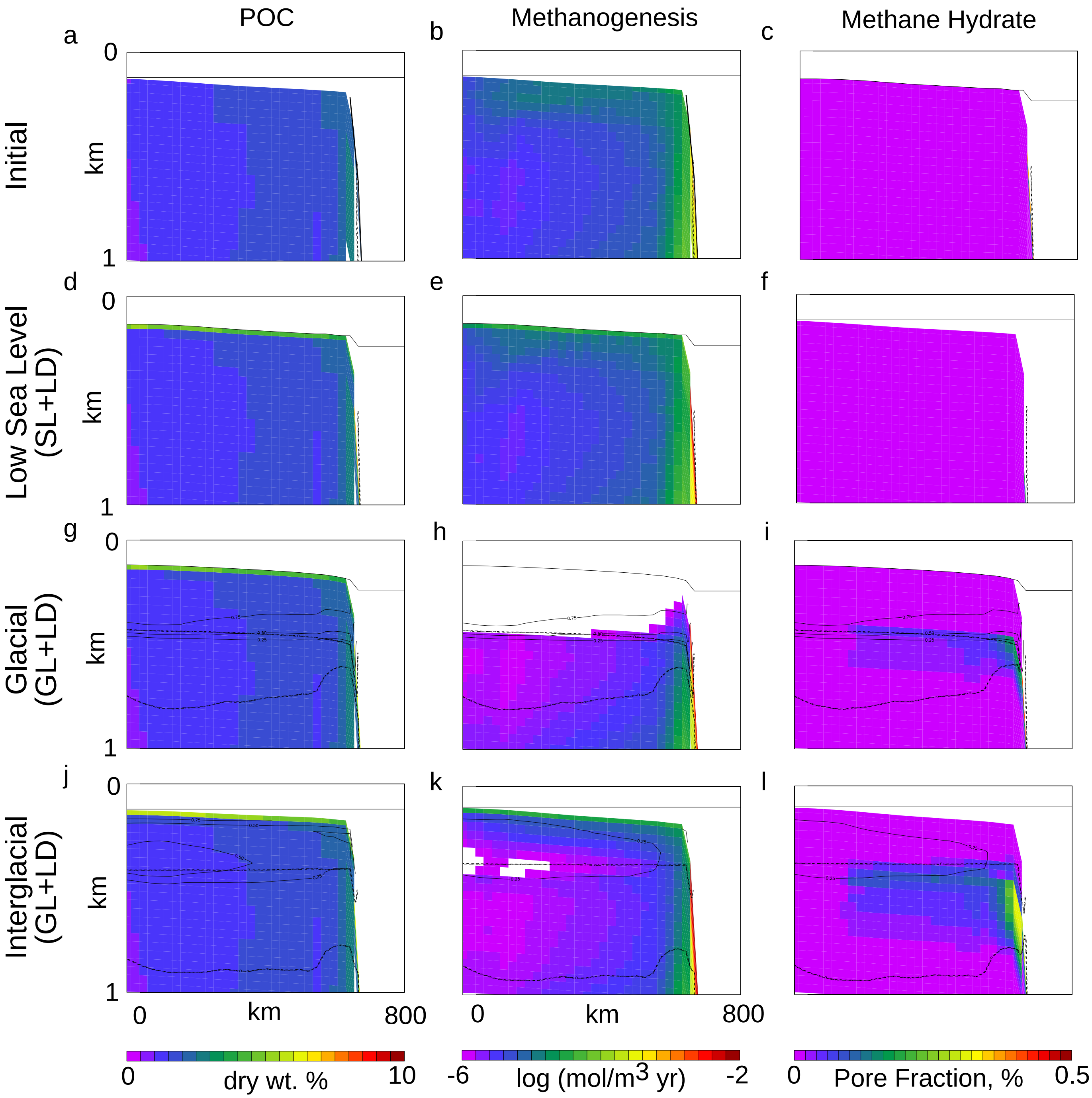
POC
Methanogenesis
Methane Hydrate
a
b
c
d
e
f
g
h
i
j
k
l
Initial
Low Sea Level
(SL+LD)
Glacial
(GL+LD)
Interglacial
(GL+LD)
0
1
km
0
km
800
0
dry wt. %
10
-6
log (mol/m3 yr)
-2
0
Pore Fraction, %
0.5

Figure 14

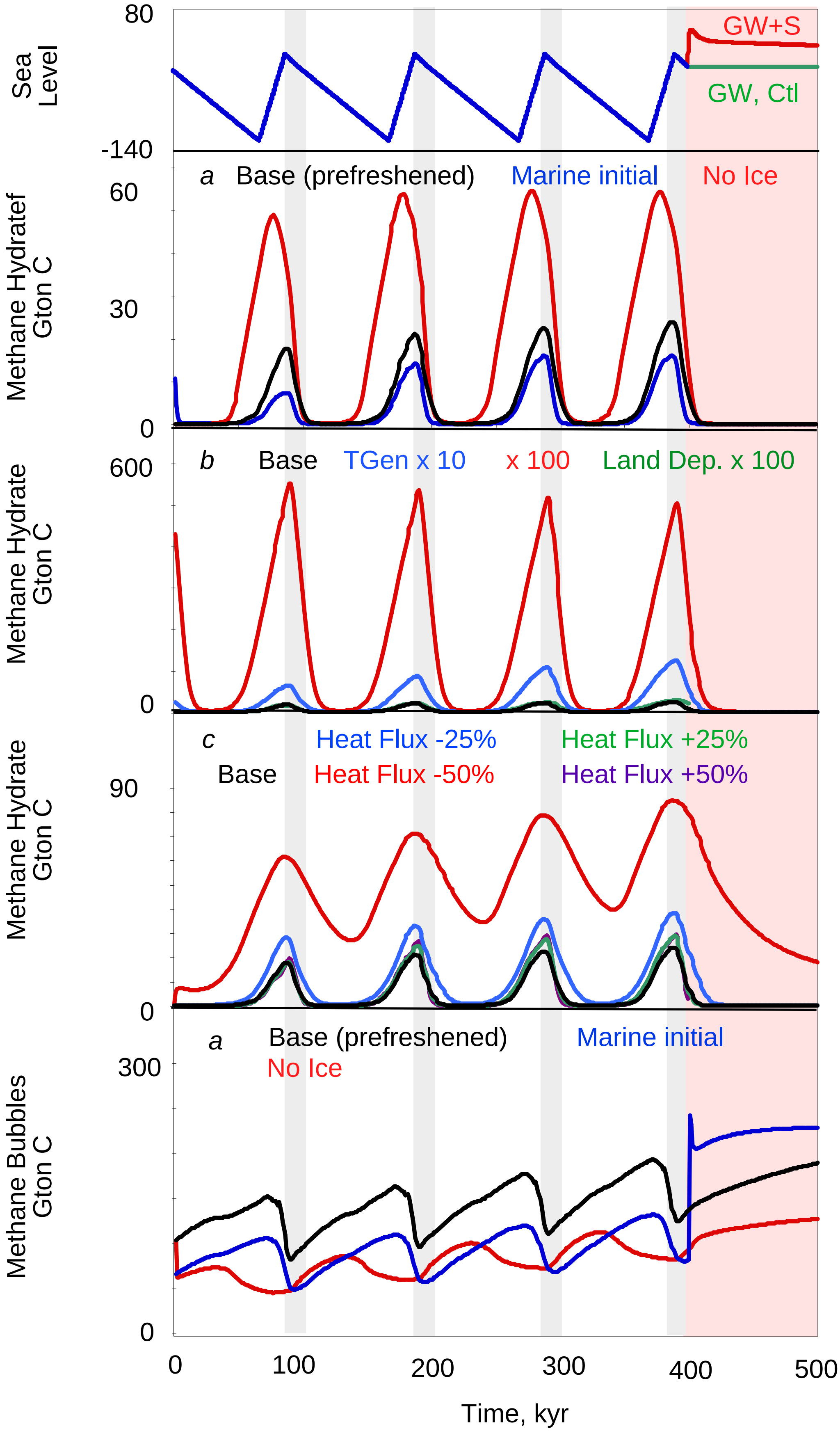

80
-140
Sea Level
GW+S
GW, Ctl
a
Base (prefreshened)
Marine initial
No Ice
60
30
0
Methane Hydratef Gton C
b
Base
TGen x 10
x 100
Land Dep. x 100
600
0
Methane Hydrate Gton C
c
Heat Flux -25%
Heat Flux +25%
Base
Heat Flux -50%
Heat Flux +50%
90
0
Methane Hydrate Gton C
a
Base (prefreshened)
Marine initial
No Ice
300
0
Methane Bubbles Gton C
0
100
200
300
400
500
Time, kyr

Figure 15

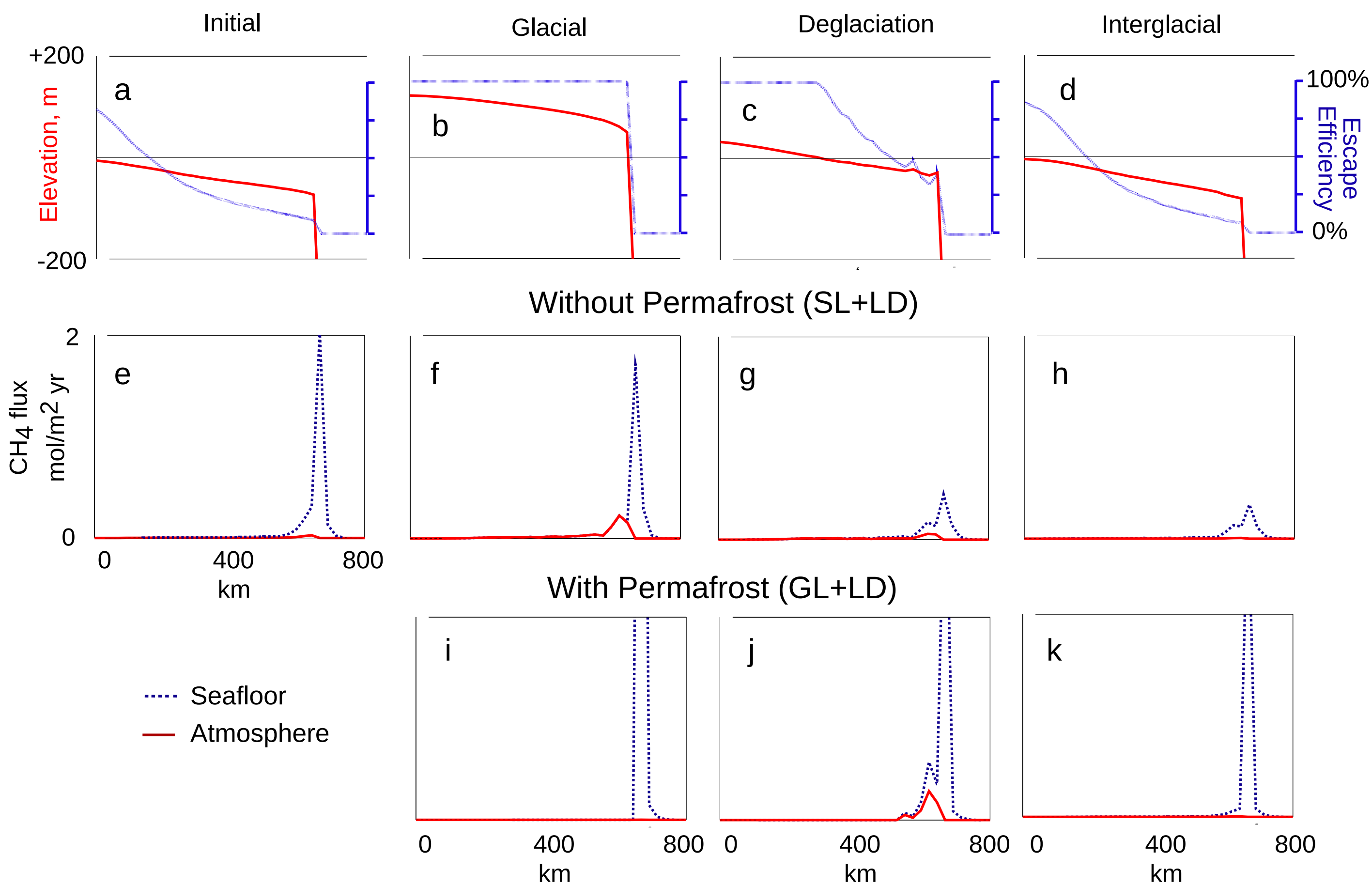
Initial
Glacial
Deglaciation
Interglacial
+200
-200
Elevation, m
a
b
c
d
100%
0%
Escape Efficiency
Without Permafrost (SL+LD)
2
0
CH4 flux mol/m2 yr
e
f
g
h
0
400
800
km
With Permafrost (GL+LD)
i
j
k
Seafloor
Atmosphere

Figure 16

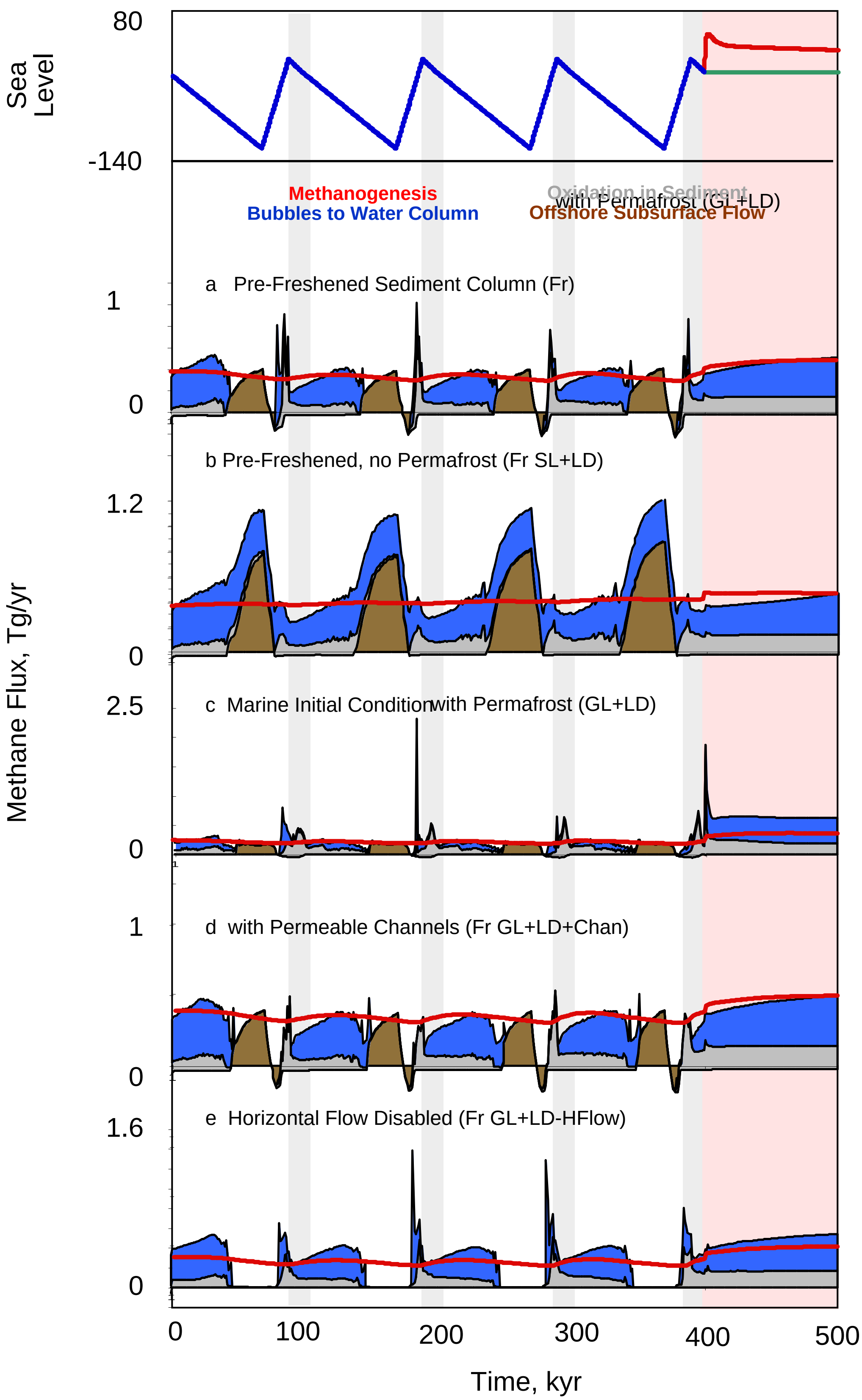
Sea Level
80
-140
Methanogenesis
Bubbles to Water Column
Oxidation in Sediment
Offshore Subsurface Flow
with Permafrost (GL+LD)
Methane Flux, Tg/yr
a Pre-Freshened Sediment Column (Fr)
1
0
b Pre-Freshened, no Permafrost (Fr SL+LD)
1.2
0
c Marine Initial Condition with Permafrost (GL+LD)
2.5
0
d with Permeable Channels (Fr GL+LD+Chan)
1
0
e Horizontal Flow Disabled (Fr GL+LD-HFlow)
1.6
0
0
100
200
300
400
500
Time, kyr

Figure 17

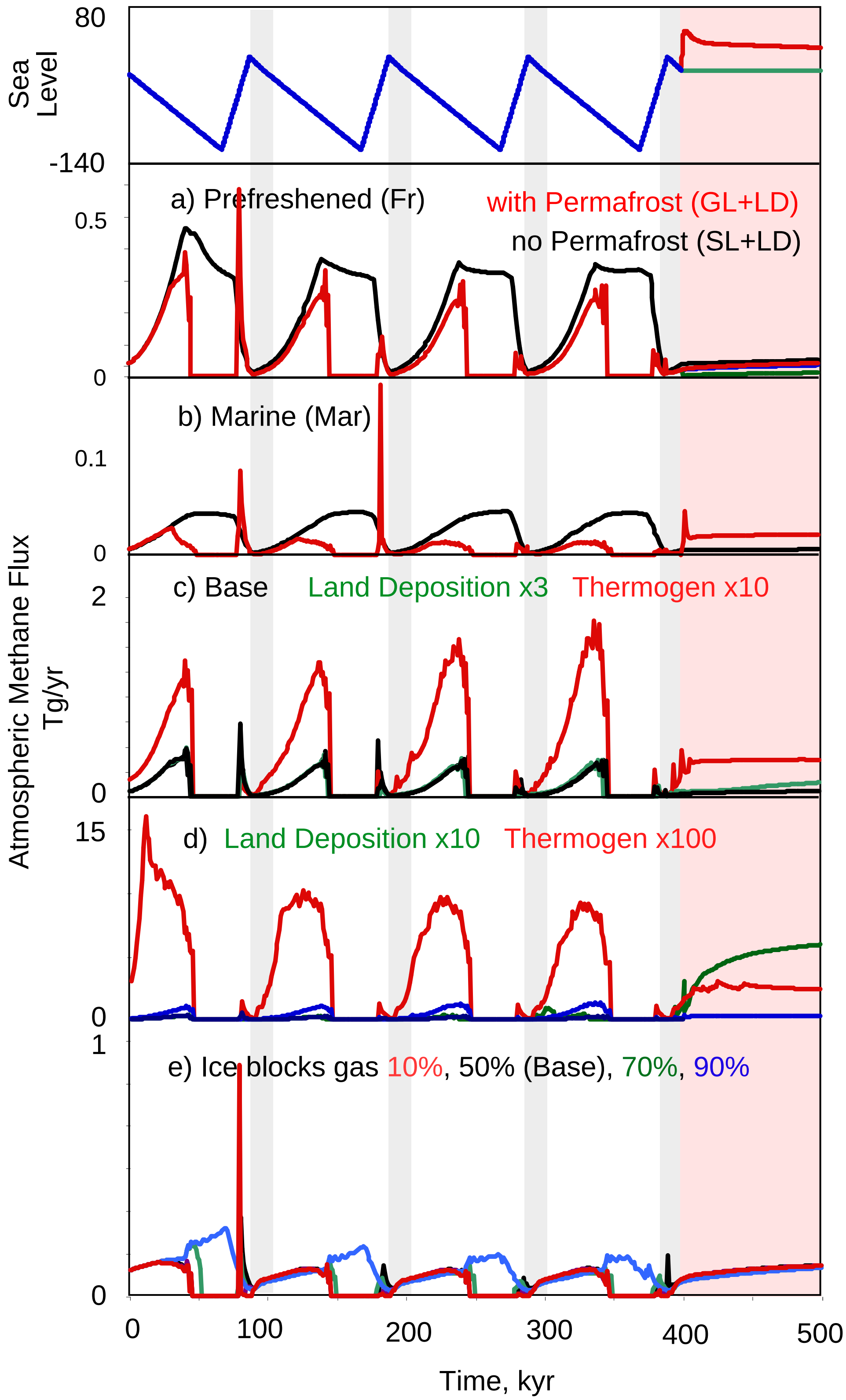
80
-140
Sea Level
a) Prefreshened (Fr)
with Permafrost (GL+LD)
no Permafrost (SL+LD)
0.5
0
b) Marine (Mar)
0.1
0
c) Base
Land Deposition x3
Thermogen x10
2
0
d) Land Deposition x10
Thermogen x100
15
0
1
e) Ice blocks gas 10%, 50% (Base), 70%, 90%
0
Atmospheric Methane Flux
Tg/yr
0
100
200
300
400
500
Time, kyr

Figure 18

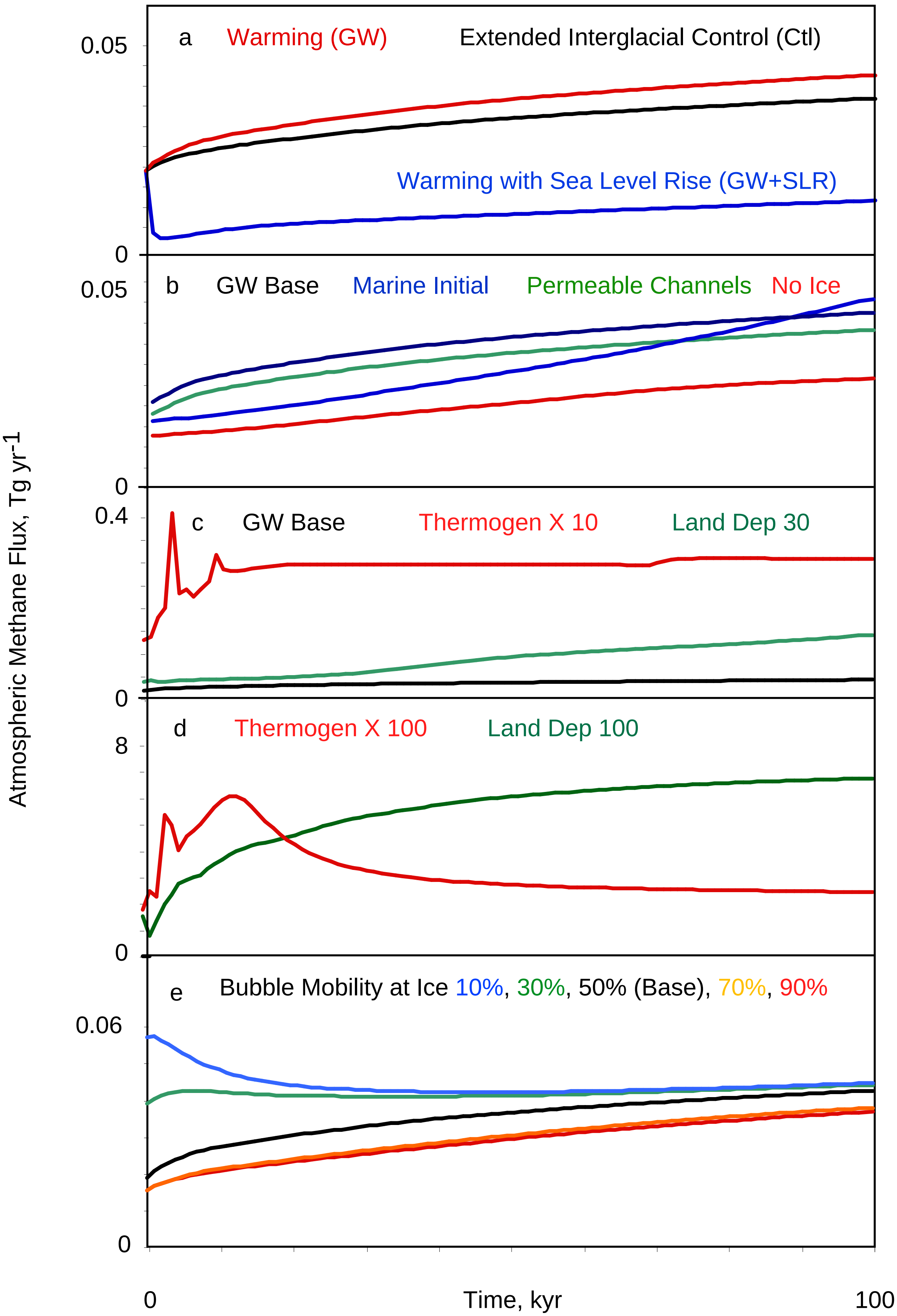

Atmospheric Methane Flux, Tg yr-1
a
Warming (GW)
Extended Interglacial Control (Ctl)
Warming with Sea Level Rise (GW+SLR)
0.05
0
b
GW Base
Marine Initial
Permeable Channels
No Ice
0.05
0
c
GW Base
Thermogen X 10
Land Dep 30
0.4
0
d
Thermogen X 100
Land Dep 100
8
0
e
Bubble Mobility at Ice 10%, 30%, 50% (Base), 70%, 90%
0.06
0
0
Time, kyr
100

Figure 19